Universidad Carlos III de Madrid

Departamento de Bioingeniería e Ingeniería Aeroespacial

TRABAJO FIN DE GRADO

SETTING UP A C-ARM FOR ITS USE AS A TOMOGRAPH

Autor:
Alba García Santos

Director:
Mónica Abella García

Co-Director:
Claudia de Molina Gómez

Leganés, 9 de Julio de 2015.

SETTING UP A C-ARM FOR ITS USE AS A TOMOGRAPH

AUTOR: Alba García santos

DIRECTOR: Mónica Abella García

CO-DIRECTOR: Claudia de Molina Gómez

**Departamento de Bioingeniería e Ingeniería Aeroespacial
Universidad Carlos III de Madrid**

**Laboratorio de Imagen Médica (LIM)
Unidad de Medicina y Cirugía Experimental (UMCE)
Hospital General Universitario Gregorio Marañón**

Título: Setting up a C-arm for its use as a tomograph

Autor: Alba García Santos

Director: Mónica Abella García

Co-director: Claudia de Molina Gómez

EL TRIBUNAL

Presidente: Sara Guerrero Aspizua

Vocal: Dhiraj Kumar

Secretario: Carlos León Canseco

Realizado el acto de defensa y lectura del Trabajo Fin de Grado el día 9 de julio de 2015, en la Escuela Politécnica Superior de la Universidad Carlos III de Madrid, acuerda otorgarle la CALIFICACIÓN de:

VOCAL

SECRETARIO   **PRESIDENTE**

AGRADECIMIENTOS

Un buen proyecto al igual que un buen plato en cocina, para ser perfecto, no solo depende del cocinero, sino también de la calidad de los ingredientes.

Eso sí, en primer lugar, alguien tenía que invitarme a la cocina. Por eso, quiero agradecer a Manolo esas prácticas de empresa que me dieron la oportunidad de conocer a este gran grupo de profesionales que forman el LIM.

También quiero dar las gracias a Mónica, quien en ningún momento a lo largo de este camino ha dudado en ofrecerme su ayuda y resolver cualquier problema que me pudiera surgir, convirtiéndose en el ingrediente esencial que ha dado sabor a este plato.

A Claudia e Inés, por esas radiaciones de nuestro particular horno que tanto nos han quemado. Pero sobre todo, por ser el cuchillo y la tijera que me han ayudado a hacer los problemas más pequeños para poder cocinarlos mejor, estando ahí siempre que he necesitado consejo o ayuda, mil gracias.

¿Y qué es un buen plato sin salero y picardía? Gracias a Aurora e Iván, por ser mi sal y mi pimienta que me alegraban esos días en los que se me quemaba la comida.

Y no podemos olvidar la base de toda cocina, el aceite, indispensable para preparar la comida pero que a la hora de la presentación no se ve ni una gotita. Por eso quiero agradecer a Laura su apoyo cuando estaba atrancada , que sin tener nada que ver con mi proyecto, incluso en algunas ocasiones sin saber la respuesta a la pregunta, me ayudaba a encontrar soluciones, gracias por dejar tu huella invisible.

A mis otros compañeros de la escuela de cocina, por saber lo que significa quemar un plato y tener que trasnochar para arreglarlo. Porque solo vosotros podéis hacer momentos de biblioteca y de trabajos inolvidables. Y aunque hasta ahora solo hayan sido cuatro años de amistad, espero que sigan siendo muchos más, sois muy grandes.

Tampoco puede faltar la lechuga y los tomates de mi ensalada, mis amigas de toda la vida, que me han dado esa frescura y color en esos momentos de agobio en los que solo necesitaba hablar y darme una vuelta, gracias por estar ahí en todo momento.

Y finalmente, no puedo olvidar a mi familia que ha sido la llama que ha mantenido viva y encendida la cocina, no solo durante este proyecto sino durante toda mi vida, apoyándome y animándome en los momentos de debilidad en las que las cosas no siempre salían como una espera, haciendo que todo fuera más fácil y pudiendo finalmente llegar a lo que hoy me he convertido, muchas gracias por todo, os quiero.

ABSTRACT

The work included in this thesis is framed on one of the lines of research carried out by the *Biomedical Imaging and Instrumentation* group from the *Bioengineering and Aerospace Department of Universidad Carlos III de Madrid* working jointly with the Gregorio Marañón Hospital. Its goal is to design and develop a new generation of Radiology Systems, valid for clinical and veterinary applications, through the research and development of innovative technologies in advanced image processing oriented to increase image quality, to reduce dose and to incorporate tomography capabilities. The latter will allow bringing tomography to situations in which a CT system is not allowable, due to cost issues or when the patient cannot be moved (for instance, during surgery or ICU). It may also be relevant to reduce the radiation dose delivered to the patient, if we can obtain a tomographic image from fewer projections than using a CT.

In that context, this thesis deals with incorporating tomography capabilities in a system originally design for planar images: the SIREMOBIL C-arm developed by SIEMENS. The system consists of an X-ray generator and a detector mounted in an arc-shaped wheeled base that allows a great variety of movements.

The use of this C-arm for tomography presents several difficulties: (1) the detector is an image intensifier which is an analog detector with image distortions, (2) the system may have mechanical strains changing the relative positions of the source and detector, and (3) the movements of source-detector pair may differ from a circular path. To obtain good quality images, it is necessary to design a new acquisition protocol that solves the effects of these non-idealities including an exhaustive calibration of the system, not needed when it is used for planar imaging.

First a calibration algorithm has been adapted to the system under study. Besides the mechanical calibration of the source and detector relative positions, it is necessary to obtain the angular position of the complete system. This work presents the effects of errors in the angle estimation and describes the implementation of a positioning system that obtains the angular position with the required precision for a tomographic

reconstruction. A digital detector has also been incorporated to the system to solve the drawbacks of the image intensifier together with the development of a software tool to transform the data acquired into in the appropriate format for the reconstruction software.

Evaluation of the proposed acquisition protocol on phantoms and rodent data show the feasibility of the proposal.

Part of this project has generated a scientific publication and was presented as an oral communication at the *Congreso Anual de la Sociedad Española de Ingeniería Biomédica (CASEIB)*. Finally, it should be noted that the work of this thesis has a clear application in industry, since it is part of a proof of concept of the new generation of C-arm systems which will be commercialized worldwide by the company SEDECAL.

KEYWORDS

C-Arm, X-Ray Imaging, Computed Tomography, Calibration

RESUMEN

El trabajo presentado en esta tesis forma parte de una línea de investigación llevada a cabo por el Grupo de Instrumentación e imagen Médica del departamento de Bioingeniería y Aeroespaciales de la Universidad Carlos III de Madrid en colaboración con el Hospital Gregorio Marañón. Tiene por objetivo el diseño y desarrollo de una nueva generación de sistemas radiológicos, con aplicación tanto en clínica como en veterinaria, a través de la investigación y el desarrollo de las nuevas tecnologías orientadas a la mejora de la calidad de la imagen, con el fin de reducir la dosis recibida por el paciente e incorporar capacidades tomográficas. Esta última característica permitiría el uso de la tomografía en situaciones en las que no es posible utilizar un sistema TAC, ya sea por razones económicas o porque el paciente no puede ser desplazado (por ejemplo, durante una cirugía o porque se encuentra en la UCI). Otro punto relevante sería la reducción de la dosis de radiación recibida por el paciente, al poder obtener imágenes tomográficas usando menos proyecciones que utilizando un TAC.

En este contexto, esta tesis trata de incorporar capacidades tomográficas a un sistema originalmente diseñado para obtener imágenes planas, en particular, el arco en C SIREMOBIL desarrollado por SIEMENS. Este sistema consta de una fuente de rayos X y un detector montados sobre una base con forma de arco que permite una gran variedad de movimientos.

El uso de este arco en C como tomógrafo presenta varias dificultades: (1) el detector es un intensificador de imagen, que es un detector analógico que presenta distorsiones en la imagen, (2) el sistema puede presentar deformaciones mecánicas que resultan en el cambio de la posición relativa de la fuente y el detector, y (3) los movimientos del conjunto fuente-detector pueden diferir de una trayectoria circular. Para obtener imágenes de buena calidad, es necesario diseñar un nuevo protocolo de adquisición que solucione los efectos de estas deficiencias incluyendo una calibración exhaustiva del sistema, no necesaria cuando es usado para obtener imágenes planas.

En primer lugar, se ha adaptado un algoritmo de calibración al sistema en estudio. Además de la calibración mecánica de la posición relativa de la fuente y del detector, es necesario obtener la posición angular del sistema en su conjunto. Este trabajo presenta los efectos de errores en la estimación de la posición angular y describe la implementación de un sistema de posicionamiento que obtiene la posición angular con la precisión necesaria para llevar a cabo una reconstrucción tomográfica. Un detector digital ha sido también incorporado al sistema para solucionar los inconvenientes derivados del intensificador de imagen. Además, se ha desarrollado un software que permite adaptar los datos adquiridos al formato utilizado por el software de reconstrucción.

Resultados de la evaluación del protocolo de adquisición propuesto en un maniquí de calibración y en un roedor muestran la viabilidad de la propuesta.

Parte de este proyecto ha generado una publicación científica que ha sido presentada como comunicación oral en el *Congreso Anual de la Sociedad Española de Ingeniería Biomédica (CASEIB)*. Finalmente, cabe destacar que el trabajo de esta tesis tiene una clara aplicación industrial, ya que forma parte de una prueba de concepto de la nueva generación de sistemas de arco en C que comercializará la empresa SEDECAL en todo el mundo.

PALABRAS CLAVE

Arco en C, Imagen de rayos-X, Tomografía Axial Computarizada, Calibración

INDEX OF CONTENTS

INDEX OF FIGURES

INDEX OF TABLES

1. INTRODUCTION

1.1 Introduction to X-ray

X-rays were discovered by Wilhelm Konrad Röntgen in 1895 while he was experimenting with cathode tubes. In these experiments, he used fluorescent screens, which start glowing when struck by light emitted from the tube. To Röntgen's surprise, this effect persisted even when the tube was placed in a carton box. He soon realized that the tube was emitting not only light, but also a new kind of radiation, which he called X-rays because of their mysterious nature. This new kind of radiation could not only travel through the box. Röntgen found out that it was attenuated in a different way by various kinds of materials and that it could, like light, be captured on a photographic plate. This opened up the way for its use in medicine. The first "Röntgen picture" of a hand was made soon after the discovery of X-rays. No more than a few months later, radiographs were already used in clinical practice. The nature of X-rays as short-wave electromagnetic radiation was established by Max von Laue in 1912.

X-rays are electromagnetic waves. Electromagnetic radiation consists of photons. The energy *E* of a photon with frequency *f* and wavelength λ is:

$$E = \frac{h \cdot c}{\lambda}$$

where *h* is Planck's constant and *c* is the speed of light in vacuum; $hc = 1.2397 \times 10^{-6}$ eV m. The electromagnetic spectrum (see Figure 1.1) can be divided into several bands, starting with very long radio waves, extending over microwaves, infrared, visible and ultraviolet light, X-rays, used in radiography, up to the ultrashort-wave, high energetic γ-rays. The wavelength for X-rays is on the order of Angstrøms (10^{-10}m) and, consequently, the corresponding photon energies are on the order of keV (1 eV = 1.602 × 10−19 J). In medical imaging, X-ray photons of energies between 10 keV and 150 keV are used [1]**.**When working with X-ray between 10 eV and 30 keV, are called "soft" and are used in microscopy.
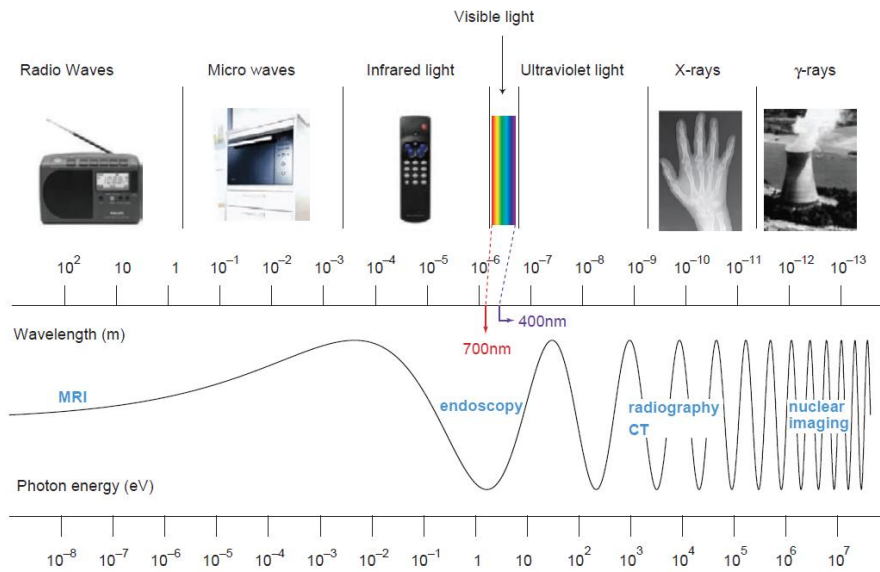
Figure 1. 1 Electromagnetic spectrum and X-ray position.

1.2 Generation of X-rays

X-rays are generated in an *X-ray tube*, which consists of a vacuum tube with a *cathode* and an *anode* (Figure 1.2). The cathode current releases electrons at the cathode by thermal excitation [2]. These electrons are accelerated toward the anode by a high voltage applied between the cathode and the anode. The electrons hit the anode and release their kinetic energy mainly as heat and only a 4% as X-ray photons.
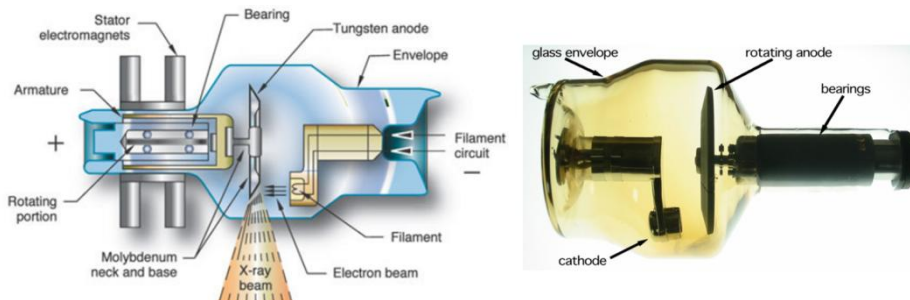
Figure 1. 2 (Left) Sketch of an X-ray tube. (Right) Typically rotating anode X-ray tube.

When the electrons hit the target, X-rays are created by two different atomic processes:

bremsstrahlung and *characteristic radiation*. Bremsstrahlung yields a continuous X-ray spectrum while characteristic radiation yields characteristic peaks superimposed onto the continuous spectrum (Figure 1.3)[3]

- ***Bremsstrahlung or braking radiation***: occurs only when the incident electron interacts with the force field of the nucleus. The incident electron must have enough energy to pass through the orbital shells and approach the nucleus of the atom. Due to the positive charge of the nucleus, the incident electron slows down and changes its course. As a result, the electron loses energy and changes direction.

- ***Characteristic radiation***: The energy of the electrons at the cathode can release an orbital electron from a shell (e.g., the K-shell), leaving a hole. This hole can be refilled when an electron of higher energy (e.g., from the L-shell or the M-shell) drops into the hole while emitting photons of a very specific energy. The energy of the photon is the difference between the energies of the two electron states; for example, when an electron from the L-shell (with energy E_L) drops into the K-shell (getting energy E_k) a photon of energy

$$E = E_L - E_k$$

is emitted. Such transitions therefore yield characteristic peaks in the X-ray spectrum.
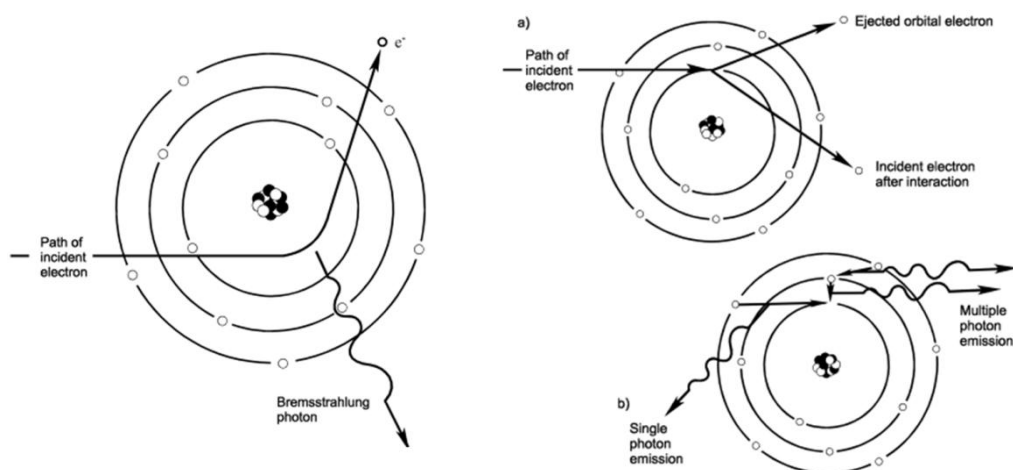
Figure 1. 3 Sketch of the processes involved in the generation of X-rays: (Left) Bremsstrahlung and (Right) characteristic radiation (a) Ejection of orbital electrons. (b) Emission of characteristic photons.
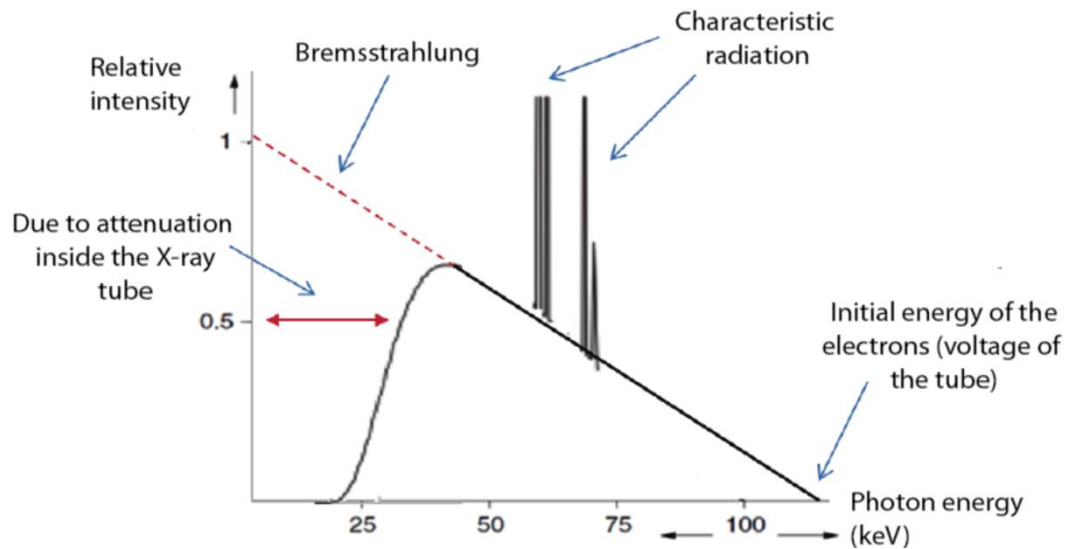
Figure 1. 4 Characteristic form of the X-ray emission spectrum due to the typical phenomena that occur in the X-ray tube. Source: [1].

The important parameters of an X-ray source are the following.

- The amount of electrons hitting the anode and, consequently, the amount of emitted photons controlled by the cathode current multiplied by the time the current is on.

- The energy of the electrons hitting the anodes and, consequently, the energy of the emitted photons controlled by the voltage between cathode and anode.

- The total incident energy at the anode, defined by the product of the voltage, the cathode current and the time the current is on.

1.2.1 X-ray interaction with matter

X-ray photons are able to ionize an atom, i.e. to release an electron from the atom. Photons with energy less than 13.6 eV are nonionizing. These photons cannot eject an electron from its atom, but are only able to raise it to a higher energy shell, a process called *excitation*. In the energy spectrum commonly used in radiology (10-150 keV), ionizing photons can interact with matter in different ways.

Mass Attenuation Coefficients for Soft Tissue
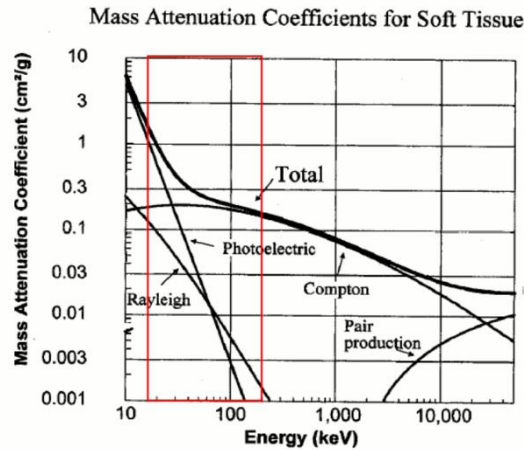
Figure 1. 5 Diagram of the different phenomena produced by the interacting X-ray photons with soft tissue (photoelectric effect, Compton, Rayleigh and pair production) as a function of the energy of these photons. The red box shows the energy range (keV) used in medical imaging where photoelectric effect, Rayleigh and Compton are present.

These processes occur due to the following phenomena (see Figure 1.6):

· The energy of X-ray photons can be absorbed by an atom and immediately released again in the form of a new photon with the same energy but traveling in a different direction. This nonionizing process is called *Rayleigh scattering* or *coherent scattering* and occurs mainly at low energies (<30 keV).

· A photon can be absorbed by an atom while its energy excites an electron. The electron then escapes from its nucleus in the same direction as the incoming photon was traveling. This mechanism is called *photoelectric absorption*.

· Other possibility is that the photon transfers only part of its energy to eject an electron with a certain kinetic energy. In that case, a photon of the remaining lower energy is emitted and its direction deviates from the direction of the incoming photon. The electron then escapes in another direction. This process is called *Compton scattering*.
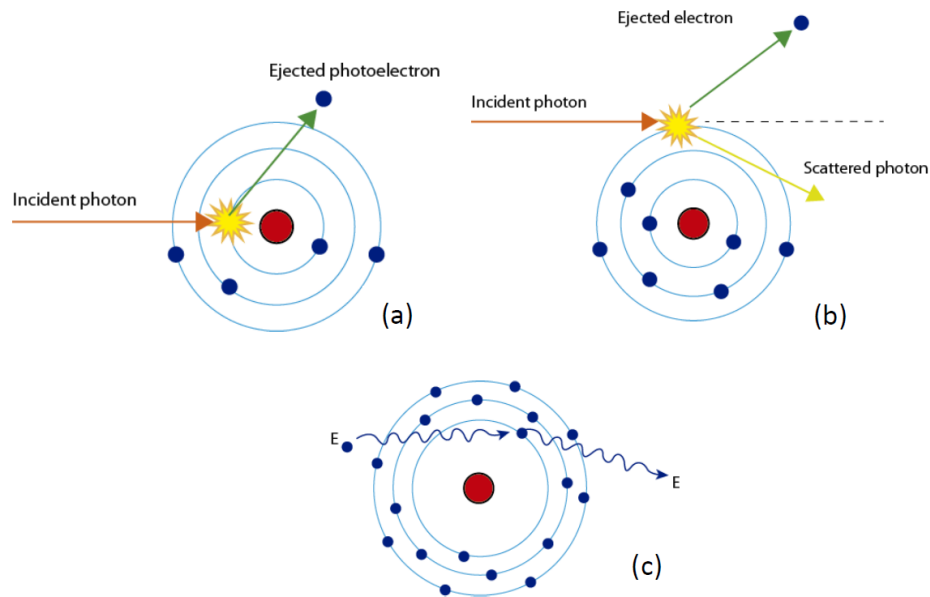
Figure 1. 6 Diagrams of the processes that occur when X-ray photons interact with matter: (a) Photoelectric effect, (b) Compton effect and (c) Rayleigh effect.

1.2.2 Scatter reduction

Scatter radiation is produced during a Compton interaction. In this interaction, a primary photon interacts with an outer-shell electron and changes direction, thereby becoming a scattered photon. Scattered photons are not a part of the useful beam and will impair image quality by placing exposures on the image receptor that are unrelated to patient anatomy.

1.2.2.1 Beam Collimation

Beam collimation consists on the reduction of the size of the surface area on the patient exposed by the primary beam. Beam collimation improves the quality of the radiograph by decreasing the amount of scatter radiation. However, when the beam is restricted, less scatter radiation will reach the image receptor and, as a result, technical factors may need to be increased to compensate for the reduction in the overall image receptor exposure.

Beam restriction can be carried out using different devices:

Aperture diaphragm

It is a flat sheet of metal, usually lead, with an opening cut in the center and attached to the X-ray tube port. It is simple and low cost, used in special procedures angiography studies.
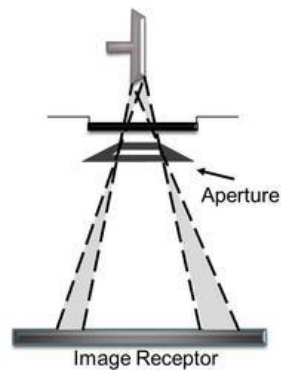
Figure 1. 7 Aperture diaphragm.

Cone/Cylinder

They are essentially circular aperture diaphragms with metal extensions. A cone has a extension that flares or diverges, with the upper diameter smaller than the bottom flared end, and a cylinder does not flare. They are simple and low cost, but their main disadvantage is the fixed field size. They are rarely used today.
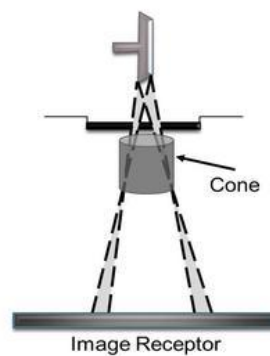
Figure 1. 8 Cone/cylinder.

Collimator

It is the most widely used beam restrictor. A collimator permits an infinite number of field sizes. It also has the advantage of providing a light source to the radiographer as an aid in properly placing the tube and central ray. Automatic collimators are

Hospital General Universitario
Gregorio Marañón
Comunidad de Madrid
SaludMadrid

Universidad
Carlos III de Madrid

electronically interlocked with the Bucky tray so the X-ray beam is automatically restricted to the size of the cassette.
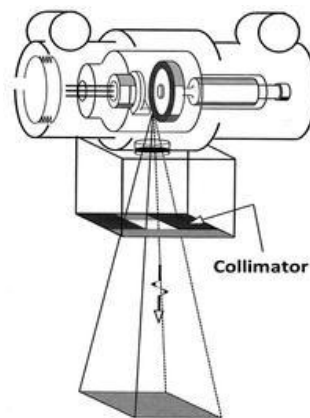
Figure 1. 9 Collimator.

1.2.2.2   Air Gap

This method consists of separating the patient's body and the receptor surface. This allows the reduction of some scattering radiation that would not reach the detector due to that separation.
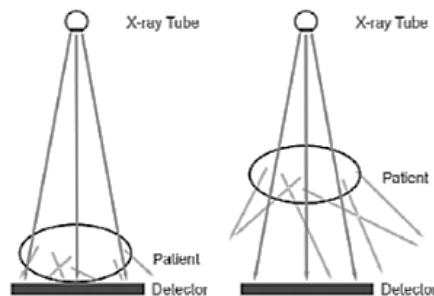
Figure 1. 10 Scatter reduction by air gap.

1.2.2.3   Grids

A grid is a device that is placed in front of the detector to absorb the scattered radiation before it can reach the image receptor.

Because a grid is designed to absorb the unwanted scatter radiation, it is especially important when imaging thicker-larger body parts and with procedures that require higher-kVp techniques.

A grid is made of a radiopaque septa (radiopaque strips) separated by radiolucent interspace material. The radiopaque septa needs to absorb the scatter radiation and

Hospital General Universitario
Gregorio Marañón
Comunidad de Madrid
SaludMadrid

Universidad
Carlos III de Madrid

must therefore be made of a dense material with a high atomic number. Lead is the material of choice because it is inexpensive and easy to make thin strips. The interspace material must be radiolucent (allows radiation to pass easily through).
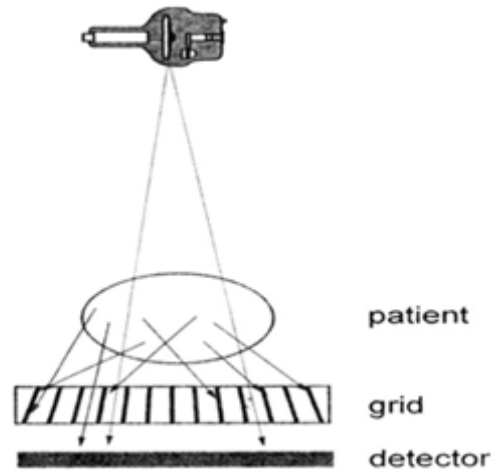
Figure 1. 11 Scatter elimination using a grid.

1.2.3 X-Ray detection

To produce an image from the attenuated X-ray beam, the X-rays need to be captured and converted to image information. The first X-ray detectors used in medicine were based on photographic film covered by a silver emulsion. Photographic film is very inefficient for capturing X-rays. Only 2% of the incoming X-ray photons contribute to the output image on a film. The low sensitivity of film for X-rays would yield prohibitively large patient doses. Therefore, an intensifying screen is used in front of the film (Figure 1.12). When X-rays interact with the fluorescent screen, light photons are released to excite the photographic film. This reduces the amount of radiation needed to obtain a good quality image, decreasing X-ray dose to the patient.
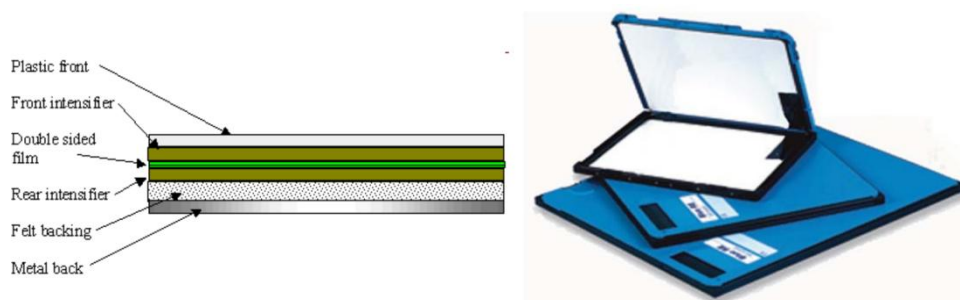
Figure 1. 12(Left) Cross section representation of a film covered on both sides by a fluorescent screen and (Right)example of commercial intensifier screen.

Computed radiography (CR) substitutes the screen-film combination by a photostimulable storage phosphor imaging plate (PSP) in the 80'.

The image formation occurs when electrons jump from valence band to conduction band as a result of photoelectric interactions, and these electrons are trapped by the impurities in the scintillator (latent image). The latent image is stored for long time (~8h after the acquisition it lose about 25%).

The latent image is processed by loading the cassette into an image reader device (IRD) where the imaging plate is scanned by a helium-neon laser beam. These laser beam scans produces the phosphors to emit the stored latent energy in the form of light photons, which are detected by photosensitive receptors and converted to an electrical signal, which is in turn converted to a unique digital value for that level of luminescence (analog-to-digital converter). Finally, the remaining energy is erased with strong light. The complete process is outlined in Figure 1.13**.**
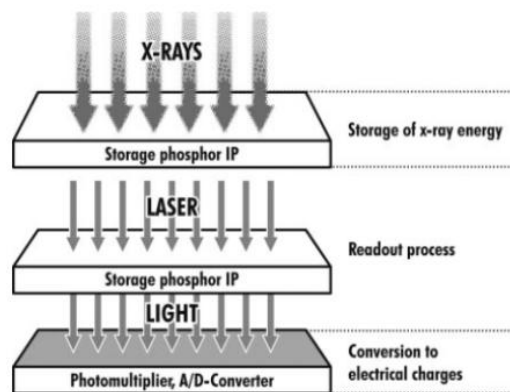
Figure 1. 13 Composition diagram of a CR digital detection system. Source: [17].

Other type of X-ray detector is the image intensifier (Figure 1.14). It is a large image tube that converts a low intensity X-ray image into a visible image. X-rays incident on an image intensifier are transmitted through an aluminum metal input window with high X-ray transmittance and less scattering. They are then absorbed by an input phosphor screen (cesium iodide crystal) and converted into a light image. On the inner surface of the input phosphor screen, a photocathode is formed, where the light image is converted into a photoelectron image. The photoelectron image is then accelerated and focused by an electric lens (electric field) consisting of an input window, focused

electrodes and an anode to collide with an output phosphor screen. The output phosphor screen then, again, converts this photoelectron into a visible light image. Since the photoelectron image is condensed by the electric lens to increase the density of electrons and simultaneously accelerated by a high electric field to collide with the output phosphor screen, the output image is approximately ten thousand times brighter than it would be obtained when the phosphor screen is placed at the input surface position of the X-ray image intensifier. These parts are all mounted in a high vacuum environment within glass or more recently, metal/ceramic.
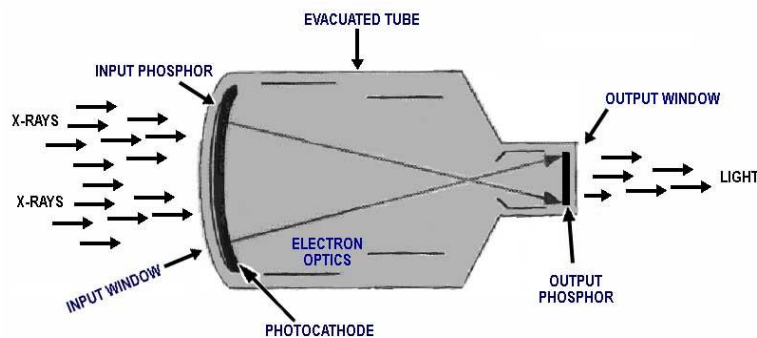
Figure 1. 14 Components of an image intensifier tube.

Once the output image is obtained, viewing of the data was via mirrors and optical systems until the adaptation of television systems in the 1960s. The output can now be captured on a camera using pulsed outputs from an X-ray tube similar to a normal radiographic exposure.

CR still requires multiple steps for the technologist, so other approaches have come up. Flat panel detector digital systems (DR) have eliminated cassettes and have reduced the number of steps to perform exams. DR systems use either direct or indirect detector (Figure 1.15).

- **Direct detectors** directly covert incoming X-ray photons to an electronic digital signal.
- In **indirect conversion** (e.g. flat panel detectors), X-ray photons are first converted into visible light proportionally to the detected photons and then these light photons are converted into electrical charges by a photodiode array.
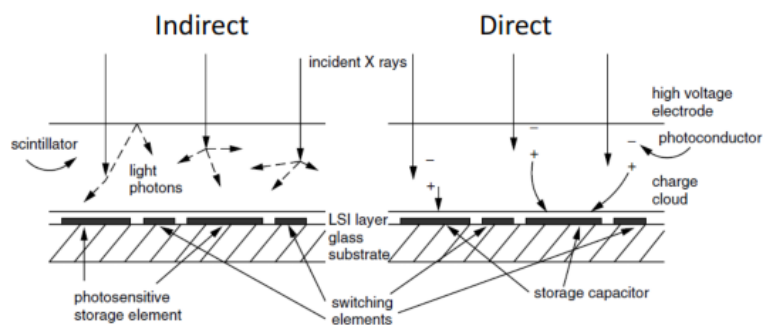
Figure 1. 15 (Left) Indirect conversion. (Right) Direct conversion.

1.3 Fluoroscopy system

1.3.1 C-arm

A mobile C-arm is a medical imaging device that is based on X-ray technology and can be used flexibly in various operating rooms within a clinic. The name is derived from the C-shaped arm used to connect the X-ray source and X-ray detector to one another.

A C-arm comprises a generator (X-ray source) and an image intensifier or flat-panel detector. The C-shaped connecting element allows movement horizontally, vertically and around the swivel axes, so that X-ray images of the patient can be produced from almost any angle. The generator emits X-rays that penetrate the patient's body. The image intensifier or detector converts the X-rays into a visible image that is displayed on the C-arm monitor. It is designed to obtain planar images.

It is a fluoroscopy system, which means that real-time moving images can be obtained. This is useful for both diagnosis and therapy and occurs in general radiology, interventional radiology, and image-guided surgery.

Figure 1. 16 Example of a C-arm.

1.4 Tomography systems

The origin of the word "tomography" is from the Greek word "tomé" meaning "slice" or "section" and "grafos" meaning "drawing." A CT imaging system produces cross-sectional images or "slices" of anatomy.

Depending on the detector shape, there are three possible configurations: parallel beam, fan beam and cone beam geometry (Figure 1.17). Parallel beam refers to a source and a 1-element detector moving in parallel with small increments to fill in one projection line. Then the pair source-detector rotated around the object under study to obtain a new projection line in different projection angles. Fan beam geometry was developed in order to make a good use of the radiation emitted by the tube in directions different from the perpendicular to a certain plane and reduce the number of displacements of source and detector, the 1-element detector evolved into a line of detector elements. In this type of systems the paths described by the rays are not parallel anymore, but diverge from the same point forming the shape of a fan. The idea of fan-beam was extended to three dimensions in order to have faster acquisitions. Using the rays emitted in all directions the detector became a plane. In these systems, rays pass through the body forming a cone, following the geometry known as cone-beam.
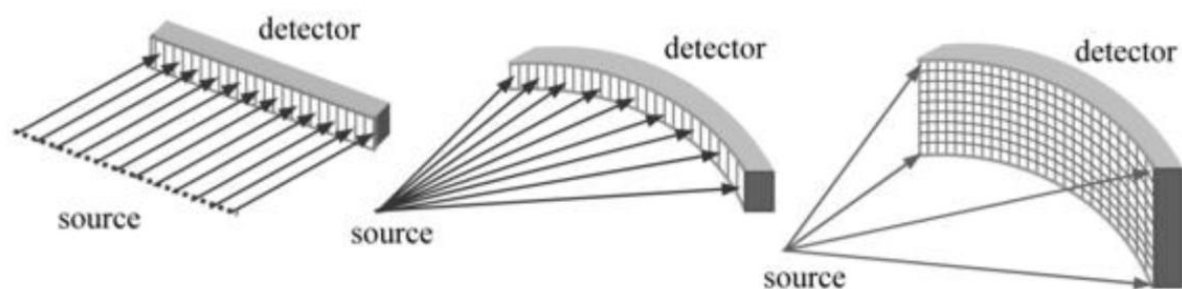
Figure 1. 17 CT geometries: (Left) parallel-beam. (Middle) fan-beam. (Right) cone-beam geometry. Source: [18].

Hospital General Universitario
Gregorio Marañón
Comunidad de Madrid
SaludMadrid

Universidad
Carlos III de Madrid

1.4.1 Projection

Data recorded on the detector is known as projection. We will start with a simple example of a 2D image with different attenuation coefficients (different values) and parallel beam geometry configuration (Figure 1.18). Projection for projection angle Ө=0 would be the sum of the attenuation coefficients through the different horizontal ray trajectories. Each projection recorded data represents the total attenuation traversed by an X-ray and t axis represents the distance of from the X-ray to the object center of coordinates. Nevertheless, this information is not enough to know the disposition and values of attenuation of the whole object. If a new projection is taken for Ө=90, we will also have information of the total attenuation through the vertical axis. For solving this simple example only two rays for two different projection angles are needed: they form a system of four equations with four unknowns. However, in a real case, the number of unknowns is greater so more projections will be needed to be able to reconstruct the object in a scanner.
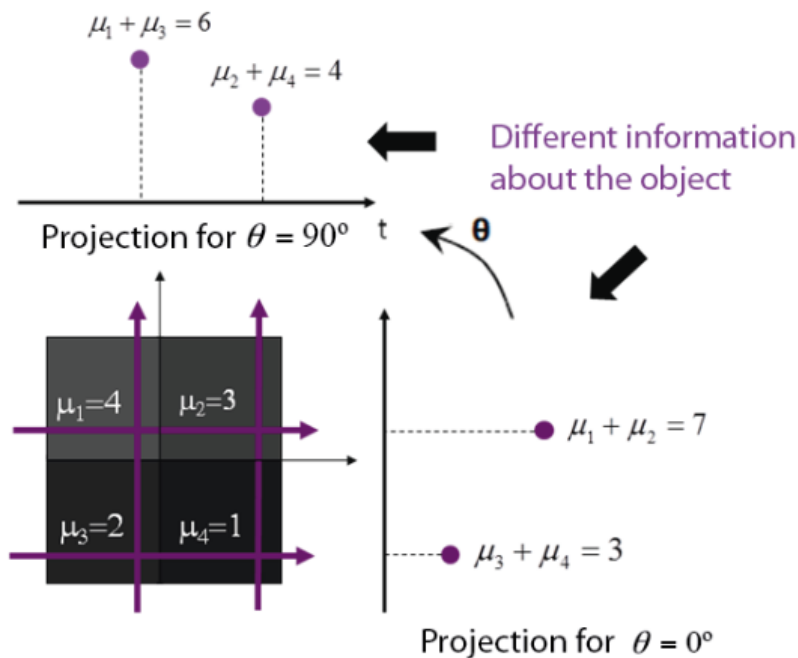
Figure 1. 18 Example to show the concept of projection.

1.4.2 Reconstruction: Methods

Image reconstruction in CT is a mathematical process that generates images from X-ray projection data acquired at many different angles around the patient. Image reconstruction has a fundamental impact on image quality and therefore on radiation dose. Two major categories of methods exist, analytical reconstruction and iterative reconstruction.

1.4.2.1 Analytical reconstruction methods

The analytical approaches for image reconstruction are based on the discretization of an idealized mathematical model in the continuous space, assuming that the projections are line integrals of the volume to reconstruct.

They assume that the projections are line integrals of the volume to reconstruct defined by the following equation for parallel rays case (Figure 1.19).

$$P_\theta(t) = \int_{(\theta,t)} f(x,y)ds = \int_{-\infty}^{\infty} f(x,y)\delta(x \cdot cos\theta + y \cdot sen\theta - t)dxdy$$

$$t = x \cdot cos\theta_0 + y \cdot sen\theta_0$$
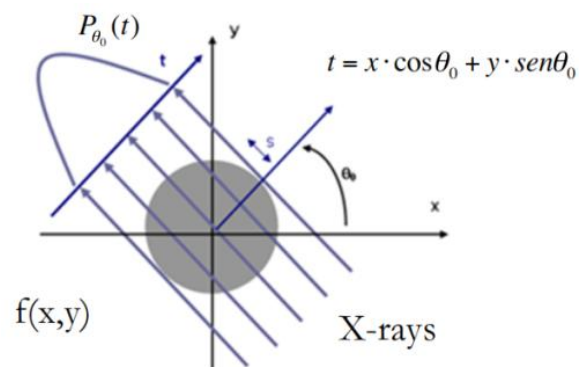
Figure 1. 19 Sketch of projection. Lines represent parallel rays that go through the object f(x,y) for projection angle θ_o and integrals along each line represent the projection value for this angle, $P_{\theta_0}(t)$.

The function $P_\theta(t)$ is known as the Radon transform of the function f(x, y). The Radon transform in two dimensions is the integral transform consisting of the integral of a function over straight lines. In other words, it is the integration of the object along the line perpendicular to the vector that joins that point to the origin. A projection is formed by combining a set of line integrals.

15

In order to establish a relationship between the projections and the object, the central slice theorem is used. It is the basis of the Radon Transform inversion. The theorem states that "Fourier transform of a parallel projection of a f(x,y) distribution for a Ɵ angle, is equal to the values of the 2D Fourier transform of a distribution in the line passing through the origin and forming the same angle with u axis" [4].Figure 1.20 illustrates the central slice theorem.
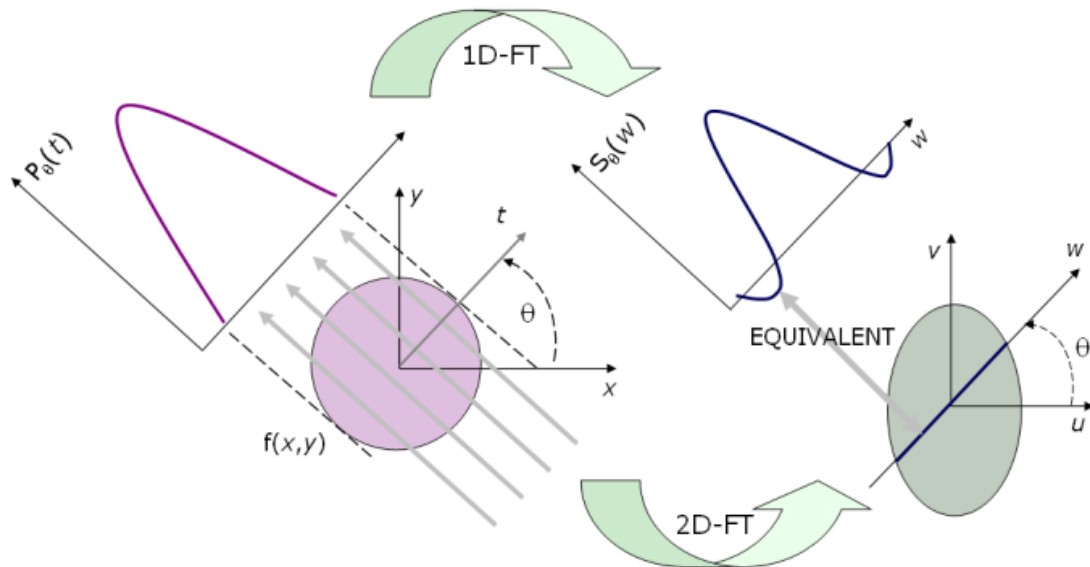
Figure 1. 20 Central slice theorem. Source: [19].

In order to invert the Radon transform to obtain the desired image, two different methods can be used: the ones based on the Fourier inverse transform and the ones based on Filtered Backprojection (FBP).

Fourier Direct Method

We can calculate the 1D Fourier transform of the projections at different angles of a certain object f(x,y) and then, using the central slice theorem, we can determine the values in the 2D Fourier transform in the object, *F(u,v)*. In the ideal case in which an infinite number of projections were taken, every point in *F(u,v)* would be known and therefore, f(x, y) could be recovered exactly using the Fourier inverse transform.

Nevertheless, in practice, a finite set of projections is available and the function *F(u, v)* is only known along a finite number of radial lines. In order to be able to use the *FFT*

(*Fast Fourier Transform),* one must then interpolate from these radial points to the points on a square grid as indicated in the middle panel of Figure 1.21. This step is the most delicate one in these methods: since the density of the radial points becomes sparser as one gets farther away from the center, the interpolation error also becomes larger. This implies that there is a higher error in the calculation of the high frequency components of an image than in the low frequency ones, which results in some image degradation.
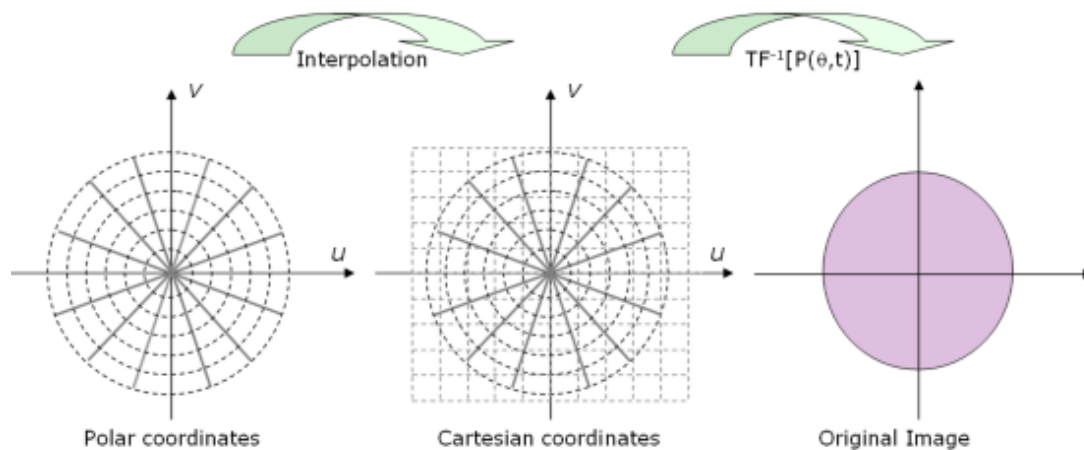
Figure 1. 21 Direct reconstructing methods. The left image corresponds with the 2D Fourier transform of the object in polar coordinates, central graphic is the same transform in Cartesian coordinates after interpolation and the image on the left represents the object, after carrying out the inverse 2D Fourier transform. Source: [19].

Filtered Backprojection

The Filtered Backprojection algorithm allows for the reconstruction of a two-dimensional function from a set of one-dimensional projections. As the name of the algorithm implies, the projections are filtered prior to backprojection.

A simple example to explain the concept of backprojection is shown in Figure 1.22. The image backprojected for the angle Ɵ= 0º is calculated by repeating the attenuation values accumulated for each of the horizontal rays. In the same way, we obtain the backprojected image for angle Ɵ= 90º. The final backprojection image will be the sum of the backprojected images for every angle.
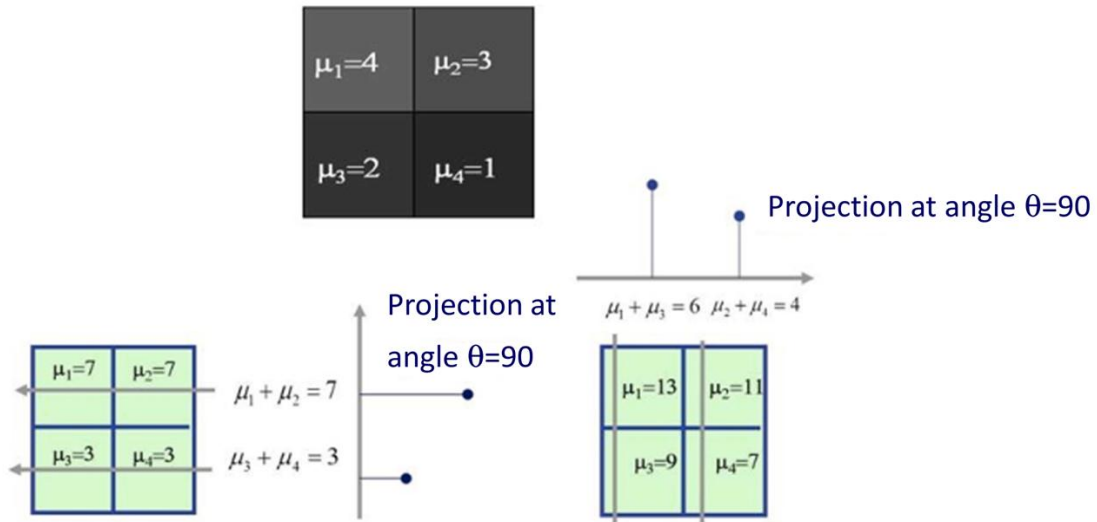
Figure 1. 22 Basic example illustrates the concept of backprojection.

As mentioned before, in a real case (with more pixels), more projections are needed. Figure 1.23 illustrates some examples from different backprojected images. The high low frequency component produces the blurring of the backprojected image. For this reason, it is needed to filter this image in order to recover the original image.
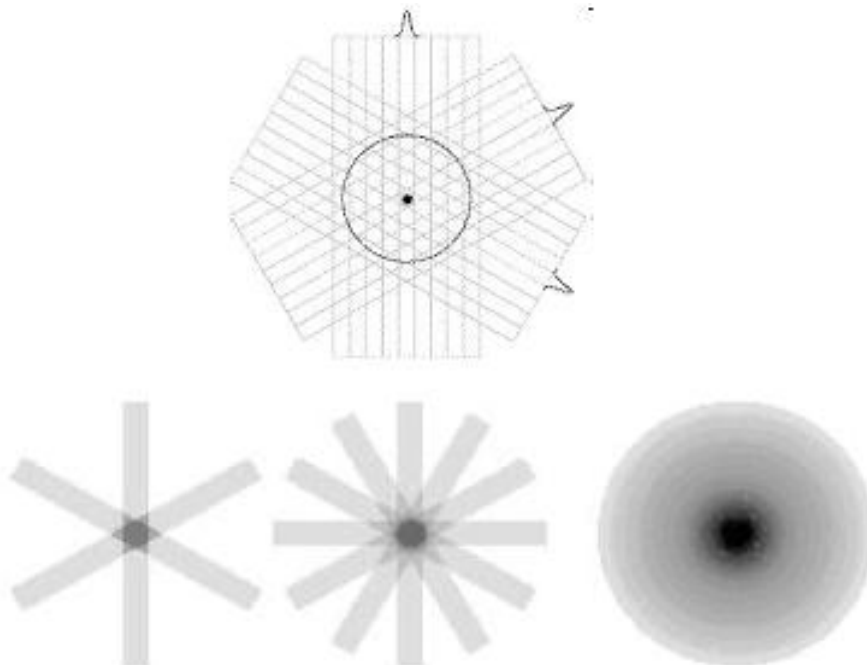
Figure 1. 23 Original image (top) consists of a single point. In the bottom part, images resulting from backprojection of 3, 6 and 360 degrees respectively are shown. In the last case, it can be seen how edges are smoother.

When the Random transform, f(t,θ), is displayed as an image with t and ,θ as rectilinear coordinates, the result is called a Sinogram. The sinogram contains the data necessary to reconstruct f(x,y). Each row of a sinogram is a projection along the corresponding angle on the vertical axis.

In Figure 1.24 can be seen the effect of applying the filter. In the case in which the sinogram is backprojection without applying the filter, the result is a blurred image with very high low frequency component. Nevertheless, if a ramp filter is applied to the initial sinogram, high frequencies are enhanced, while keeping low frequencies, resulting in better reconstruction results.
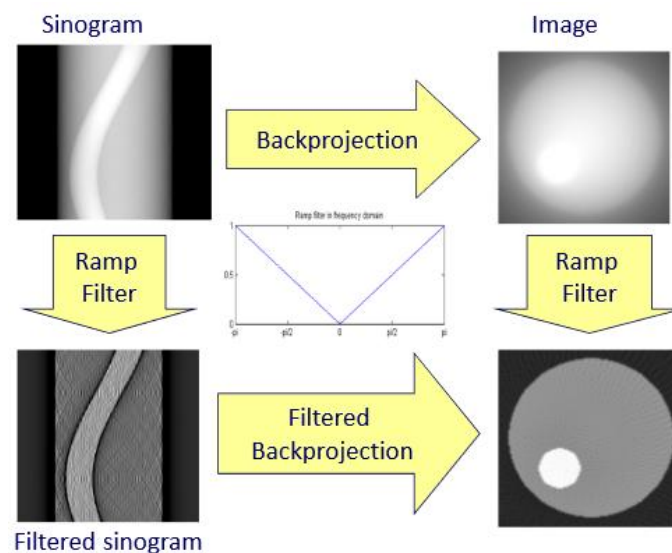
Figure 1. 24 Scheme of the different steps in the FBP and the filter effect

FDK Reconstruction

Most of the scanners for are based on cone-beam geometry with a detector orbiting in a circular path. The reconstruction of these systems is done based on the method proposed by Feldkamp, Davis and Kress algorithm method (FDK). [5]

To develop this method, the problem is studied introducing a third coordinate to the FBP reconstruction so that all rays can be considered from the proper coordinate system transformations. Furthermore, the real coordinates system is matches with the object coordinate system in order to obtain a more efficient implementation. (Figure 1.25).
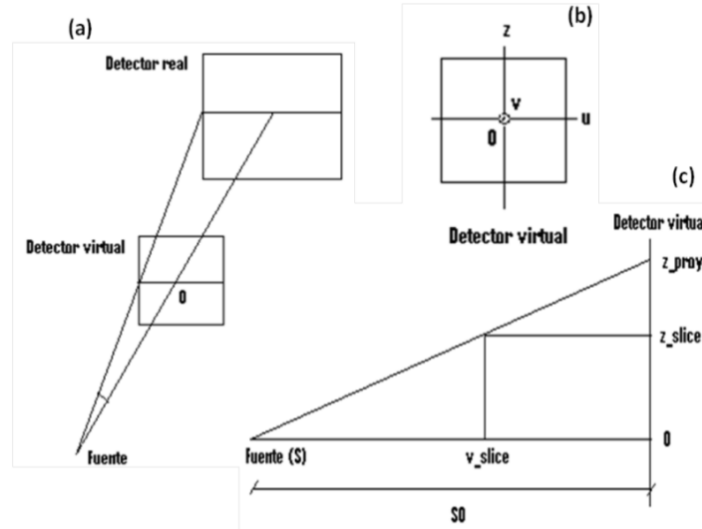
Figure 1. 25 (a) perspective view, (b) front view and (c) lateral view of cone beam geometry. For reconstruction, real detector coordinate system will be matched with virtual detector coordinate system.

The mathematical derivation of this reconstruction method results in the following equation:

$$f(u,v,z) = \frac{1}{2}\int_0^{2\pi}\frac{v_{FO}}{(v_{FO}-v)^2}\int_{-\infty}^{\infty}R_\beta(s,z)\cdot h\cdot\left(\frac{v_{FO}}{v_{FO}-v}-s\right)\frac{v_{FO}}{\sqrt{v_{FO}^2+z^2+u^2}}\,ds\,d\beta$$

In cone beam with circular trajectory, projections from every angle are obtained but with information of different planes. Using FDK, the sufficiency condition is softened since it supposes that he whole volume can be reconstructed slice by slice although the Radom space is not complete.

1.4.2.2   Iterative reconstruction methods

These methods propose a different way of solving the reconstruction. These techniques are a better, but computationally more expensive, alternative to FBP methods. The aim of these methods is to find a vector f what satisfies $p = A \cdot f$. Where p corresponds to the projections data along the different rays and A to the weights that represent the contribution of every pixel for all the different rays in the projection. The principle is to find a solution by successive estimates. In order to implement these algorithms, we first make an initial guess $f^{(0)}$ at the solution. Then we take successive projections. The projections corresponding to the current estimate

20

are compared with the measured projections. The result of the comparison is used to modify the current estimate, thereby creating a new estimate.

1.5 Artifacts in CT

The term "artifact" refers to any systematic discrepancy between the reconstructed image and the actual attenuation coefficients of the object. The CT images are more prone to artifacts than conventional radiographs because the image is reconstructed from the order of a million measures from independent detectors; reconstruction algorithms assume that all these measurements are consistent, so any measurement error will be reflected as a error in the reconstructed image.

The sources of artifacts can be classified in four categories: (1) artifact due to physics, (2) due to subject, which are caused by such factors as patient movement or the presence of metallic materials in or on the patient, (3) caused by imperfections in the scanner and (4) artifacts produced by the image reconstruction process.

1.5.1 Physics-based artifacts

1.5.1.1 Beam hardening

An X-ray beam is composed of individual photons with a range of energies. As the beam passes through an object, it becomes harder, i.e. its mean energy increases, because the lower energy photons are absorbed more rapidly than the higher energy photons. Two types of artefact can result from this effect: so-called 'cupping' artefacts and the appearance of dark bands or streaks between dense objects in the image.

There are two factors involved in the origin of beam hardening: the attenuation coefficients dependency on energy and the polyenergetic nature of the X-ray source beam. . As the beam passes through an object, it becomes harder, i.e. its mean energy increases, because the lower energy photons are absorbed more rapidly than the higher energy photons. This is a direct consequence of the energy-dependence of attenuation coefficients, which are higher at lower energies. Because of this, X-ray travelling in different trajectories across an object, will emerge with different spectra, giving rise to data inconsistencies that result in reconstruction artifacts.

Two types of artefact can result from this effect: so-called 'cupping' artefacts and the appearance of dark bands or streaks between dense objects in the image. These effects are illustrated on Figure 1.26.
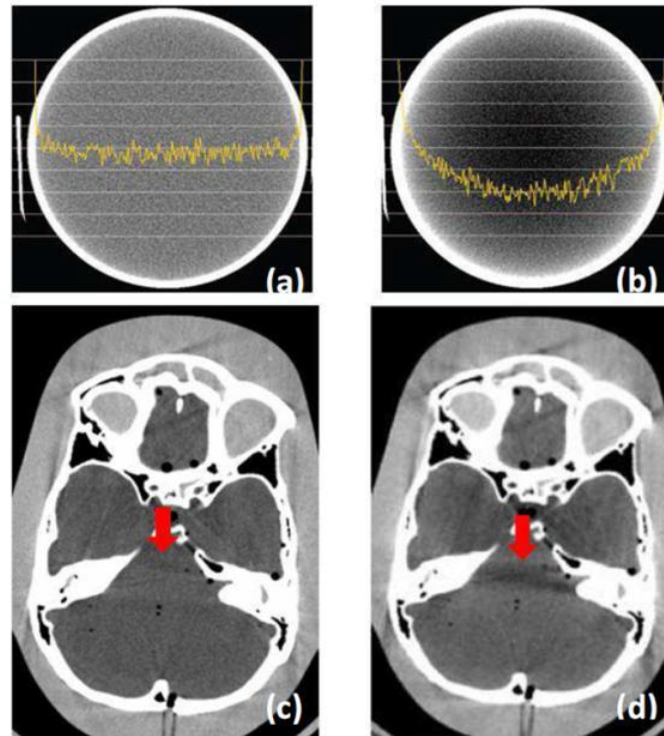
Figure 1. 26 (a) CT Axial section of a homogeneous cylinder without beam hardening in which the yellow line represents the profile across the red line, (b) same axial section with beam hardening, in which the cupping artifact can be observed; (c) axial section of brain CT without beam hardening, (d) same axial section of brain CT with beam hardening artifact; difference between these two images is highlight with the red arrow. Source: [6].

1.5.1.2 Photon starvation

When an insufficient number of photons reach the detector, a phenomenon known as photon starvation occurs.

In dense areas, many photons are absorbed and not reach the detectors, resulting in very noisy projections due to the decrease of signal to noise ratio. In the reconstructed image various artifacts, such as the white streaks observed in Figure 1.27, will appear.

Figure 1. 27 (Left) Axial and (right) coronal images showing streaking artifact due to photonstarvation Source: [6].

1.5.2 Patient-based artifacts

1.5.2.1 Metallic materials

The presence of metal objects in the field of view can introduce artifacts that degrade the image quality, as can be shown in the example in Figure 1.28**.** This is due to the high attenuation coefficient of these objects to the X-rays, which prevents signal reaches the detector.
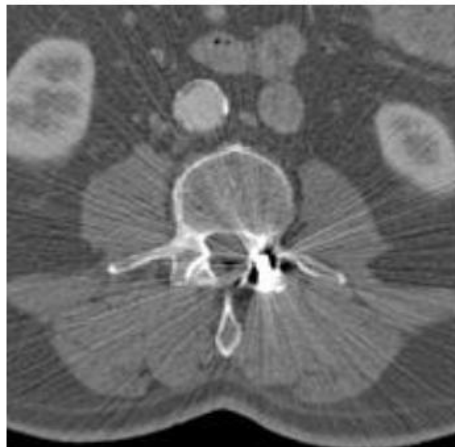
Figure 1. 28 CT image showing the appearance of artifact caused by metallic artifacts [6].

1.5.2.2 Patient motion

Potential patient motion can result in inconsistent projections, causing artifacts in reconstructed images that appear as bands in the example to the left in Figure 21**.** Moreover, involuntary movements such as breathing may cause significant artifacts in the area of the diaphragm, as is shown in the right panel of Figure 1.29**.**
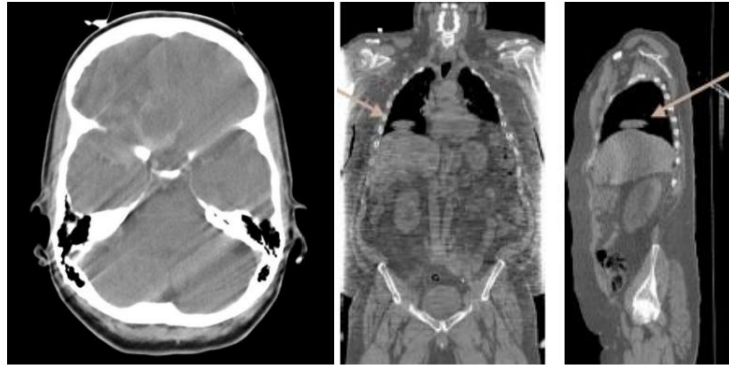
Figure 1. 29 (Left) CT image with artifacts due to patient motion. (Right) Coronal and sagittal CT image slices where the arrow points to a liver structure that is inserted into the lung due to movement of the diaphragm. Source: [6].

1.5.3 Scanner-based artifacts

1.5.3.1 Ring artifacts

In CT that uses flat-panel detectors and that describe circular paths, ring artifacts appear in the reconstructed images, which impede quantitative analysis of the images as can be seen in Figure 1.30. These artifacts are due to differences in gain at the pixel detector.
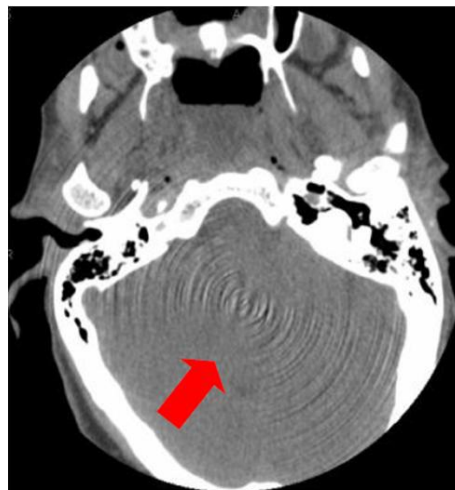
Figure 1. 30 Axial section of a brain CT image. Red arrow indicates the presence of ring artifact. Source: [6].

1.5.3.2   Mechanical artifacts

The origin of this artifact resides in tolerances in the manufacturing process, especially in the mechanical positioning of the detector. The detector can have different geometric misalignments from its ideal position in the scanner.

The possible configurations are shown in Figure 1.31: (a) Vertical and horizontal displacement of the detector; (b) rotation of the detector with respect to the z axis, parallel to detector plane columns; (c) detector tilt towards the x ray source around u axis; (d) skew of the detector in its plane.
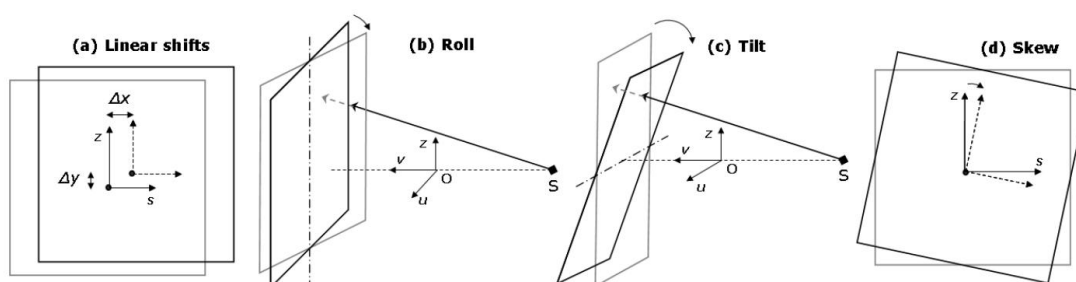
Figure 1. 31 Linear shifts, roll and tilt out of the detector plane, and skew (in the detector plane) . [z, s] and [u,v,z] are the coordinate systems in the detector and the FOV respectively and S represents the position of the X-ray source. Source: [20].

Depending on the geometric misalignment, different artifacts appear in the reconstructed image. Figure 1.32 illustrates the artifact formed in a CT image acquisition by a detector whose plane is horizontally shifted
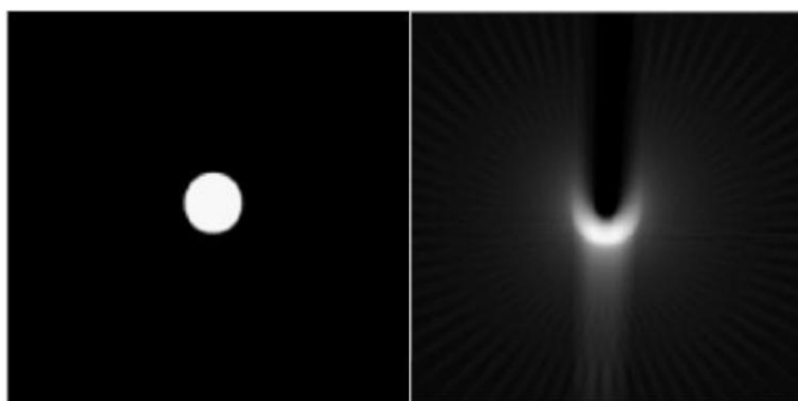
Figure 1. 32 (Left) Reconstructed image without geometric misalignment. (Right) Reconstructed image with horizontal detector displacement. Source: [21].

1.5.4 Reconstruction artifacts

1.5.4.1 Number of projections and samples

There are two important factors for reconstruction in the data acquisition: number of samples in each projection and number of projections. A small number of any of these variables may produce different kinds of artifacts in the reconstruction as can be seen in Figure 1.33: Gibbs phenomenon, bands and streaks and Moiré effect.

A large number of projections (K) and a low number of samples per projection (N), leads to significant artifacts in the form of bands due to overlap or aliasing. These artifacts occur because the projection is sampled at a number less than the Nyquist frequency, i.e. the theoretical bandwidth of the projection in Fourier space is higher than the sampling frequency.

Moreover, a low number of projections will also lead to artifacts due to lack of data acquired in the angular dimension.
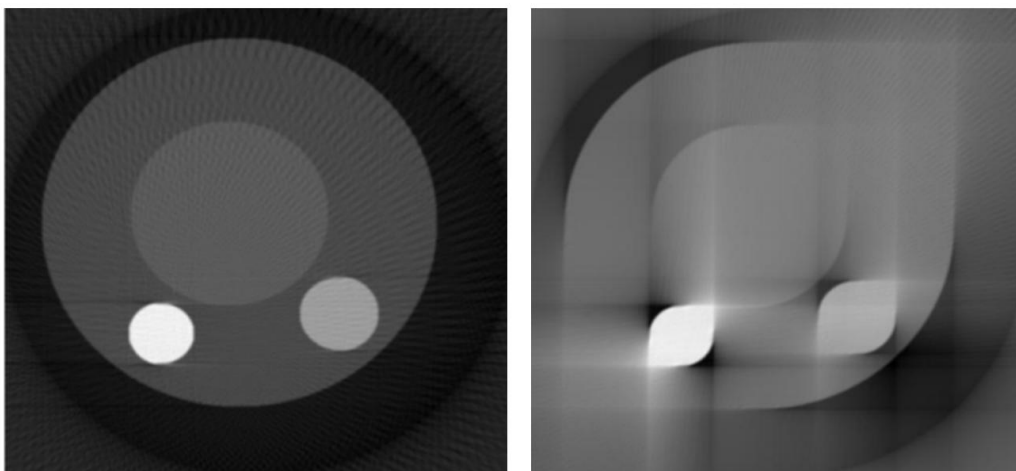
Figure 1. 33 (Left) Reconstruction with not enough number of projections. (Right) Reconstruction with a small angle span.

The number of projections should be slightly higher than the number of samples or the number of rays in each projection (in the case of parallel rays) and their relationship is determined by the following expression [4]:

$$\frac{K}{N} \cong \frac{\pi}{2}$$

1.5.4.2 Truncation artifact

If any portion of the patient lies outside the scan field of view, the computer will have incomplete information relating to this portion and streaking or shading artifacts are likely to be generated. Furthermore, if the FBP method is used to reconstruct the image, the filter step will increase the high frequencies causing bright shading in the area where the truncation has occurred. This is illustrated in Figure 1.34.

Figure 1. 34 CT image showing truncation artifact (bright shading) because of patient diameter (70 cm) was bigger than field of view (50 cm of diameter).

2. MOTIVATION AND OBJECTIVES

2.1 Motivation

In the area of radiological technologies, recent years are seeing a rapid advance towards the digital equipment. The introduction of digital detectors in conventional radiology systems not only allows an easier handling of imaging studies with PACS (Picture Archiving and Communication System), but also opens the door to a revolution in the field of so-called "Conventional" Radiology. This digitalization raises the opportunity of using advanced processing methods that convey significant advantages compared to previous technology, especially in terms of increase the contrast and dynamic range of images and, more interestingly, of obtaining studies in which the third spatial dimension is included. The latter will allow bringing tomography to situations in which a CT system is not available due to cost issues or when the patient cannot be moved (for instance, during surgery or ICU). It may also be relevant to reduce the radiation dose delivered to the patient, if we can obtain a tomographic image from fewer projections than using a CT. With this revolution, radiology equipment, which currently accounts for over 80% of imaging studies in the clinic, will have an even more important role in the near future for both the patient and the health system.

On the other hand, in the US there is a big social concern with the dose delivered to the patient, particularly important in pediatrics, which is creating a new regulation in this area with the aim of reducing to the minimum possible value the dose in radiological studies, according to the ALARA principle ("As Low As Reasonably Achievable"). Although this emphasis on reducing this dose received by the patient is not yet evident in Europe, extrapolating the trend in the US, we can expect to have an increasing (and reasonable) pressure in order that imaging systems use the lowest possible dose.

The work included in this thesis is framed on one of the lines of research carried out by the *Biomedical Imaging and Instrumentation* group from the *Bioengineering and Aerospace Department of Universidad Carlos III de Madrid* working jointly with the

Gregorio Marañón Hospital through its *Instituto de Investigación Sanitaria*. This line of research is carried out in collaboration with the company SEDECAL and has a clear orientation towards the technology transfer to the industry. Its goal is to design and develop a new generation of Radiology Systems, valid for clinical and veterinary applications, through the research and development of innovative technologies in advanced image processing oriented to increase image quality, to reduce dose and to incorporate tomography capabilities.

In that context, this thesis deals with incorporating tomography capabilities in a system originally design for planar images: the SIREMOBIL C-arm developed by SIEMENS. This system allows a great variety of movements, and its characteristic structure makes it possible to be used in intraoperative cases, as the arc can be situated around the patient lying in the bed.

2.2 Objectives

The work of this thesis is based on the SIREMOBIL C-arm developed by SIEMENS, a mobile fluoroscopy system. The system consists of an X-ray generator and a detector mounted in an arc-shaped wheeled base that allows a great variety of movements. The use of this C-arm for tomography presents several difficulties: (1) the detector is an image intensifier which is an analog detector with image distortions, (2) the system may have mechanical strains changing the relative positions of the source and detector, and (3) the movements of source-detector pair may differ from a circular path. To obtain good quality images, it is necessary to design a new acquisition protocol that solves the effects of these non-idealities, including an exhaustive calibration of the system not needed when it is used for planar imaging.

The general objective of the thesis is to set up the SIREMOBIL C-arm for its use as a tomography. This general objective can be divided into the following specific objectives:

1. To evaluate and solve the non-idealities due to an incorrect angular position
2. To develop a geometrical calibration method
3. To design an acquisition and reconstruction protocol

4. To evaluate system on real data

2.3 Outline of the manuscript

The manuscript consists on the following chapters:

- **Chapter 1: Introduction**. We describe the physical basis of the X-rays: generation, interaction with matter and detection. Then, differences between planar X-ray and CT are described together with the concepts of projection and the reconstruction.

- **Chapter 2: Motivation and objectives**. This chapter introduces the line of research in which this thesis is included and the specific objectives.

- **Chapter 3: System under study.** In this chapter we present the description of the C-arm used for this work and the solutions implemented to be able to use the system as a tomograph: the integration of a flat panel detector and the development of an accurate angular positioning system.

- **Chapter 4: Geometrical calibration.** This chapter presents the geometrical calibration method developed based on the adaptation of a calibration algorithm previously available in the laboratory. Finally the complete proposed acquisition protocol is described.

- **Chapter 5: Reconstruction.** We describe the reconstruction procedure evaluated using a calibration phantom.

- **Chapter 6: Evaluation on small animal.**

- **Chapter 7: Discussion and conclusion.**

- **Chapter 7: Limitations and future work.**

3. SYSTEM UNDER STUDY

3.1 C-arm SIREMOBIL Compact L of Siemens

The C-arm Model SIREMOBIL Compact L of Siemens is a mobile fluoroscopic system that consists of two units: the X-ray source based on a monofocal tube with a 1,4 kW generator and a 23 cm diameter circular image intensifier with an anti-diffusion grid mounted in an arc-shaped wheeled base, and the workstation unit used to visualize, store, and manipulate the images. This C-arm, shown in Figure 3.1, can perform different functions as fluoroscopy, pushed fluoroscopy and planar radiography, which are necessary for a wide variety of clinical procedures such as intraoperative visualization of bile ducts, metallic element implant, bone visualization, fluoroscopy techniques for pain treatments and insertion of catheters [7].
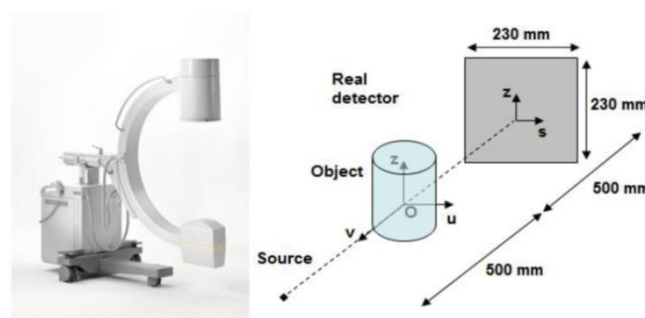
Figure 3. 1 (Left) SIEMENS C-arm. (Right) Geometry parameters of the cone-beam system.

As the C-arm system has the objective of adjusting its position to the requirements of the procedure and patient, it has handles that facilitate wide variety of movements. The whole C-arm can be horizontally freely moved when brakes are released for displacement from one place to another (Figure 3.2).

Figure 3. 2 Brakes for the different movement possibilities of the C-arm.

With the purpose of approaching to the bed regarding to its height and depth, C-arm allows 45 cm elevation from its lowest point and 20 cm horizontal displacement (Figure 3.3).
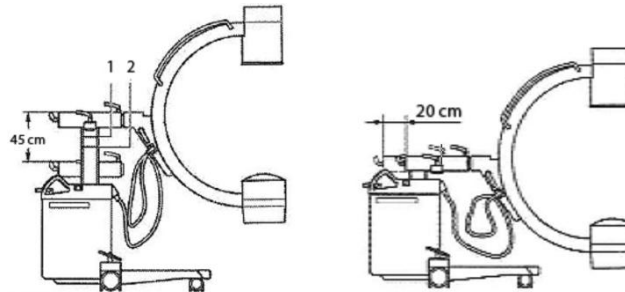
Figure 3. 3 (Left) Illustration of elevation and (Right) horizontal displacements of the C-arm.

The C-arm can rotate around two different axes in order to obtain X-ray images of the region of interest from different angular positions. We will refer to the two rotations that the system is able to perform as vertical tilt and horizontal tilt.

- Horizontal tilt is a rotation around the horizontal supporting arm and spans 360º (Figure 3.4).
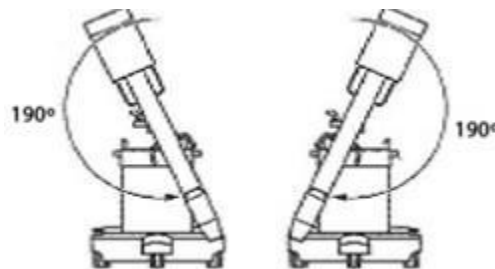
Figure 3. 4 Horizontal tilt.

- Vertical tilt consists on a rotation on the C-arm plane and spans a range from +90º to -40º starting from the neutral position (Figure 3.5). This position is reached when both the X-ray generator and the detector are aligned in the vertical plane.

Figure 3. 5 Vertical tilt.

Hospital General Universitario
Gregorio Marañón
SaludMadrid
Comunidad de Madrid

Universidad
Carlos III de Madrid
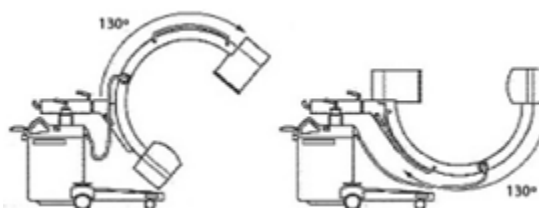
The C-arm can be rotated around the bed using one of the two turning options permitted in order to use it as a tomograph. The arc shape of the C-arm makes the vertical tilt less susceptible of suffering deformations being more stable than the horizontal tilt. Nevertheless, there is a rotation limit of 130º for this movement, which does not allow for obtaining a complete set of projections around 360 degrees, while horizontal tilt allows full rotation.

For tomography, we need to place the sample in the central point between the source and the detector, so the system can acquire projections around it. The Field of view (FOV) is defined as the image area that contains the object of interest to be measured. Due to the cone-beam geometry of the C-arm that implies a magnification of the sample, the FOV is reduced to a diameter of 11.5 cm as shown in Figure 3.6.
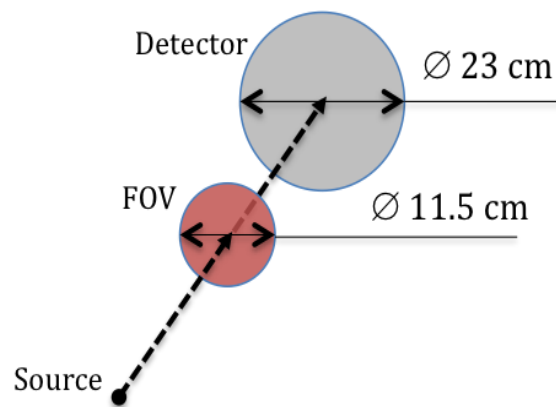
Figure 3. 6 Illustration of the dimension of the detector and the FOV of our system.

3.2 Angular positioning system

The SIREMOBIL, which is not aimed for tomography, is completely manual and only has a very rudimentary angular positioning: a scale drawn in the arm with a resolution of 5 degrees (Figure 3.7).

Figure 3. 7 Angular positioning system.

3.2.1 Effects of errors in the angular positioning

With the aim of studying the effects of errors in the angular positioning of the system on the reconstructed image, we have used a simulation tool that emulates the functioning of an X-ray system: it produces a set of projections of synthetic phantoms based on the parameters that describe the real system (shown in the right panel of Figure 3.1). This tool is implemented in CUDA language and accelerated thanks to parallel processing in Graphic Processing Units (GPUs).

We have used a synthetic phantom with similar physical characteristics to human bones and water that fits in the FOV of the C-arm under study (114.4 mm diameter). It consists of a methacrylate cylinder of 200x100 pixels, 0.8 mm pixel size with two ellipsoidal balls inside of 40 pixels diameter (Figure 3.8).
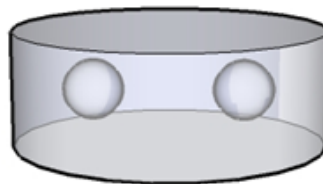
Figure 3. 8 Simulated phantom.

The number of angular positions obtained was 360, separated $1\pm\eta$ degrees, where η is a variable random error. Reconstruction was done assuming that the angular projections were obtained with 1 degree angular step in order to see the effect of an error in the angular position has on the final reconstruction.

Hospital General Universitario
Gregorio Marañón
SaludMadrid
Comunidad de Madrid

Universidad
Carlos III de Madrid

Figure 3.9 shows the effect for errors in the range of ± 1º and ±3º.
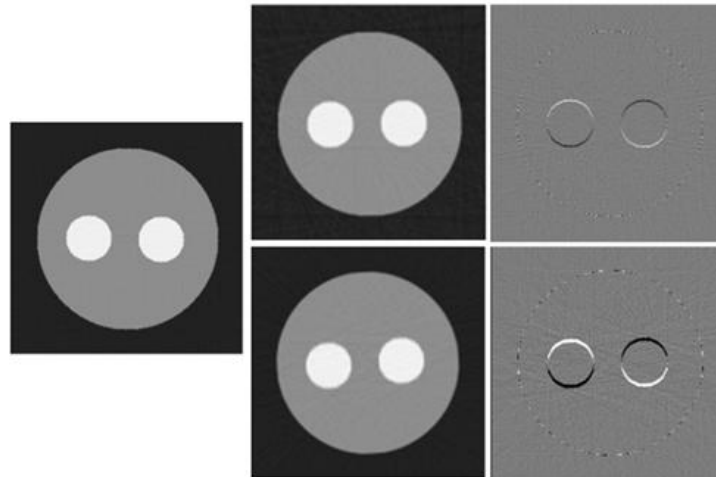
Figure 3. 9 (Left) View of the reconstructed image with no errors, (top middle) with an error in the range of ± 1º, (bottom middle) with an error in the range of ± 3 , (top right) subtraction of true image and image with error in the range of ± 1º and (bottom right) subtraction of true image and image with error in the range of ± 3º.

Errors in the angular position lower than 1 degree result on artifacts in the reconstructed images and those artifacts increase with the error.

Considering that the space between mark and mark on the scale drawn in the arc is 5º, these results indicate the need of a positioning system.

3.2.2 Positioning system

3.2.2.1 Inclinometer

We have selected the ADIS16209, a digital inclinometer with an accuracy of 0.025º. The standard supply voltage (3.3 V) and serial peripheral interface (SPI, a synchronous serial communication interface specification used for short distance communication) enable simple integration into most industrial system designs.

The ADIS16209 tilt sensing system uses gravity as its only stimulus, and a MEMS accelerometer as its sensing element.

It also incorporates the signal processing circuit that converts acceleration into an angle of inclination, and it corrects for several known sources of error that would otherwise decrease the accuracy level.

3.2.2.2   LaunchPad

To send the analog data obtained by the sensor to the computer, the model TM4C123G of LaunchPad is used. It is a single board microcontroller manufactured by Texas Instruments (Figure 3.10). In order to facilitate the development of the different applications using these LaunchPads, Energy, an open-source development environment, was used.

Figure 3. 10 Model TM4C123G of LaunchPad.

3.2.2.3   Evaluation board

To allow for the proper communication between the inclinometer and the LaunchPad we have used the ADIS1620x/PCB evaluation board that provides convenient access to the inclinometer using a standard 2 mm, 2x6, connector interface [8] (Figure 3.11).

Figure 3. 11 Inclinometer (black component) in the evaluation board.

3.2.2.4   PCB

A printed circuit board (PCB) mechanically supports and electrically connects electronic components using conductive tracks and pads from copper sheets laminated onto a non-conductive substrate.

Before the advent of the PCB circuits, the point-to-point wiring was used. In the last case, the wire routing needs to be neat and routed in such a way as to minimize interference, and the hand-soldering itself needs to be properly done. This led also to frequent failures at wire junctions and short circuits. On the other hand, using a PCB enables consistent parts placement relative to other parts, and a pre-routed wiring configuration on the PCB that reduces the potential for wiring errors.

In order to design the PCB needed to connect the evaluation board and the Launchpad, Eagle (Easily Applicable Graphical Layout Editor) was used. It consists of a schematics editor for designing circuit diagrams, a PCB editor that allows back annotation to the schematic and an auto-router module that connects traces based on the connections defined in the schematic. The software comes with an extensive library of components, but a library editor is also available to design new parts or modify existing ones. Figure 3.12 shows the schematic of the circuit been designed and Figure 3.13 shows its board layout. It was ordered to be manufactured to the company WEdirekt.
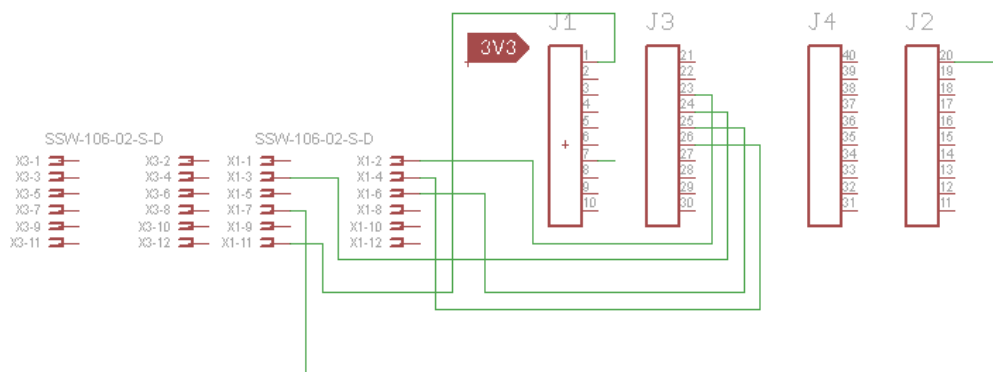
Figure 3. 12 Schematic of the circuit.
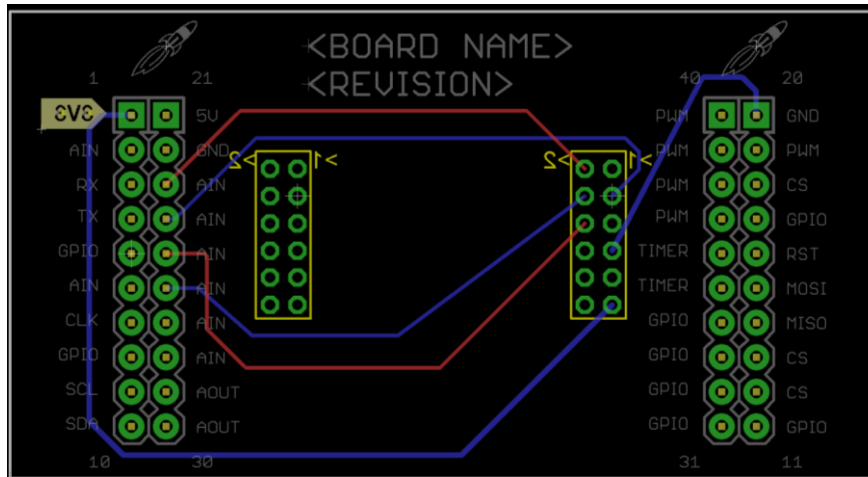
Figure 3. 13 Circuit board layout.

3.2.3 Communication between computer and inclinometer

As explained above, we use the LaunchPad as an intermediary between the inclinometer and computer. Table 3.1 shows the data configuration for each output data register in the inclinometer.

Register	Bits	Scale[1]
SUPPLY_OUT	14	0.30518 mV
XACCL_OUT	14	0.24414 mg
YACCL_OUT	14	0.24414 mg
AUX_ADC	12	0.6105 mV
TEMP_OUT	12	−0.47°C
XINCL_OUT[2]	14	0.025°
YINCL_OUT[2]	14	0.025°
ROT_OUT[3]	14	0.025°

[1] Scale denotes quantity per LSB.
[2] Range is −90° to +90°.
[3] Range is −179.975° to +180°.

Table 3. 1 Output Data Register Formats. Source:[22].

Each output data register has the following bit sequence: new data (ND) flag, error/alarm (EA) flag, followed by 14 data bits. The ND flag indicates that unread data resides in the output data registers. This flag clears and returns to 0 during an output register read sequence. It returns to 1 after the next internal sample update cycle completes. The EA flag indicates an error condition.

Since we are only interested in data regarding vertical tilt (YINC_OUT register) and horizontal tilt (XINCL_OUT register), we have developed a software using Energia IDE

to record only these data. After reading the content of one of these registers, we mask off the upper two bits (ND and EA), and convert the remaining 14-bit into a decimal equivalent and multiply by 0.025 to convert the measurement into units of angle (degrees).

3.2.4 User interaction and data storage

Data obtained cannot be stored in a file for a future use using this board, since it does not offer the possibility of creating a file. Instead, we have implemented a user interface using Processing, which is an open source programming language and integrated development environment based on Java.

The values provided by the inclinometer are in the range of ±90º for the horizontal tilt and ±180º for the vertical tilt. In the case of the vertical tilt the arc will never exceed the inclinometer's limitation of ±180º. However, for the horizontal tilt the displayed value is not correct for angles with absolute value greater than 90 degrees and this error depends on the quadrant the actual angle belongs to, as explained in Table 3.2.

	Real angle	Angle provided
0°<α<90°	65°	65°
α=90°	90°	90°
90°<α<180°	110°	70°
α=180°	180°	0°
180°<α<270°	200°	-20°
α=270°	270°	-90°
270°<α<360°	300°	-60°
α=360°	360°	0°

Table 3. 2 Examples of desired angles for the horizontal tilt and values obtained with the inclinometer.

The user interface module, apart from saving the data in a text file, transforms the angle range allowing us to visualize the actual position in consecutive angles from 0 to 360 degrees. The program also calculates the direction of rotation without user interaction depending on the initial positions in which the C-arm is moved. From the point of view of a user that changes the position of the C-arm, the movement of the horizontal tilt towards the left means positive values, whereas moving it toward the

Hospital General Universitario
Gregorio Marañón
Comunidad de Madrid
SaludMadrid

Universidad
Carlos III de Madrid

right means negative positions. When the program is initiated, the interface shown in Figure 3.14 is displayed and an empty angular position file is created.
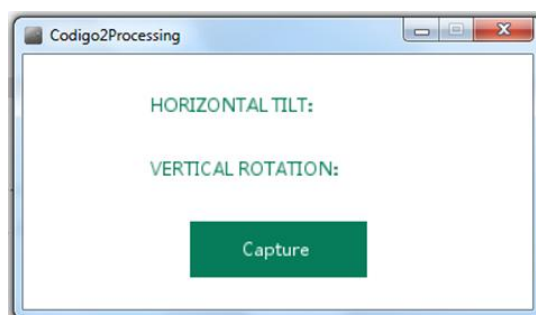
Figure 3. 14 Interface that appears when the program created in Processing is initiated.

A new line is added to the file every time the "Capture" bottom shown in Figure 3.14 is pressed. To avoid inaccuracies due to the vibration of the C-arm, the software performs an average of the last ten values read in the inclinometer when the system reaches the desired position. Figure 3.15 shows an example of the resulting angular position file.

Figure 3. 15 Angular position file.

3.2.5 Preliminary evaluation of the positioning system

When we move the arc changing the horizontal tilt, positive values will be recorded if this movement is carried out in the clockwise direction and negative values when this movement is carried out in the opposite direction from the point of view of the technician that uses the C-arm.

We have tested the developed positioning system in a real operating room to assure that it does not interfere with the C-arm movements and the normal workflow in a surgical scenario. Figure 3.16 shows the position of the inclinometer in the C-arm.

Figure 3. 16 Position of the inclinometer at top of the detector (blue arrow).

We also checked if values displayed on the computer screen matched the marks in C-arm. First, maintaining the vertical tilt, horizontal tilt was changed in both directions. We subsequently carried out the same experiment but maintaining the horizontal tilt and moving the vertical tilt. Table 3.3 shows how values obtained by the inclinometer follow the same trend that those obtained by reading the marks on the arc. Errors due to manual positioning can be solved by the inclinometer due to higher accuracy (0.025 vs. 5 degrees).
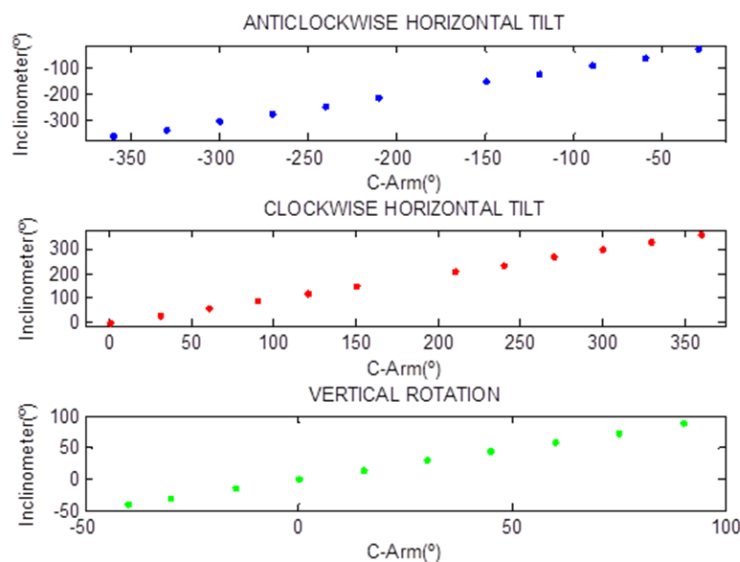
Table 3. 3 Comparison of the angles shown by the arc and the inclinometer at the same position.

3.3 Detection

The detector of the system is an X-ray image intensifier (XRII). One of the disadvantages of an image intensifier is the certain grade of line distortion and vignetting of the images that it produces, shown in Figure 3.17. This may be caused by the magnetic contamination of the image tube or by the installation of the image intensifier within a large magnetic field, which may affect the trajectory of electrons travelling inside the tube from the input phosphor screen to the output phosphor [9].
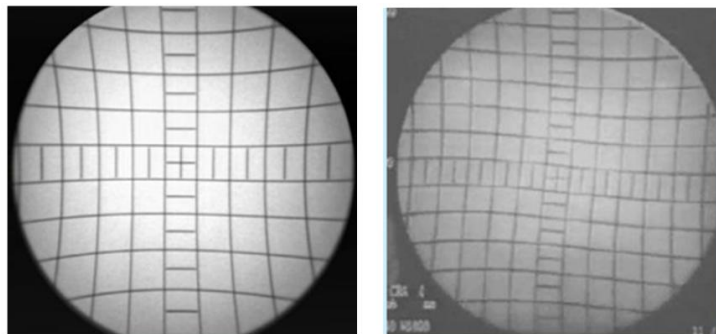
Figure 3. 17 Distortions produced by the image intensifier.

Another drawback of using this image intensifier is that it producs analog images that are displayed on the screen and we need digital images to carry out the reconstruction process.

3.3.1 Flat panel

In order to overcome the drawbacks explained previously, a digital flat-panel detector was integrated in the system.

For this work, we have selected a wireless, light weight, cassette flat panel detector for digital radiography, XRpad 4336 detector (PerkinElmer), with a pixel size of 100 µm that provides a good image quality. The XRpad is also capable of wired communication utilizing gigabit Ethernet that was used for initial configuration [10]. To acquire an X-ray image, the detector and X-ray generator must be synchronized. Using the automatic mode, the panel captures an image when it detects an X-ray flux.

.

Figure 3. 18 (Left) Wireless Router with Ethernet cable plugged into LAN port. (Right) XRpad 4336 flat panel detector.

The XRpad is operated through the X-ray Imaging Software (XIS), a user interface (Figure 3.19) that automatically detects the size of the sensor and receives images of the detector in a 16 bit digitized data format (65535 possible values). The images are presented on the screen with 256 grey levels.
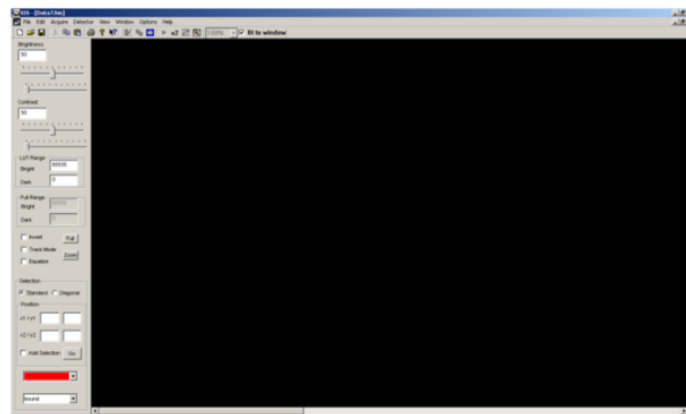
Figure 3. 19 User interface of the X-ray imaging software.

The dimensions of this detector (35×43 cm), much bigger than those of the image intensifier integrated in the C-arm (a circle of 23 cm of diameter), would enable a bigger field of view. However, the C-arm has a built-in collimator to restrict the X-ray beam to the dimensions of the original detector reducing the useful area of the flat panel to the hexagon shown in Figure 3.20.
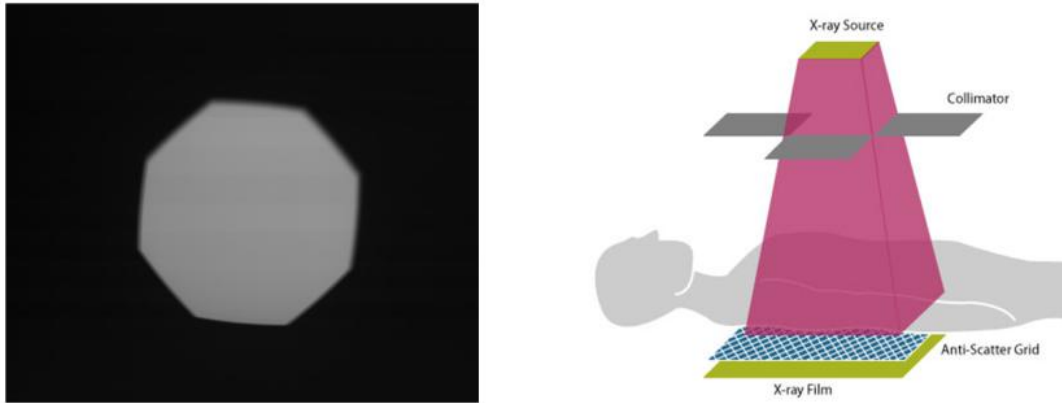
Figure 3. 20 (Left) Useful area of the flat panel detector. (Right) Illustration of a collimator function.

As explained in section 3.1, de FOV is reduced to a diameter of 11.5 cm. This small scanning area poses a problem with regard to the type of rotation movement that we can do with the C-arm since it is not isocentric in both movements.
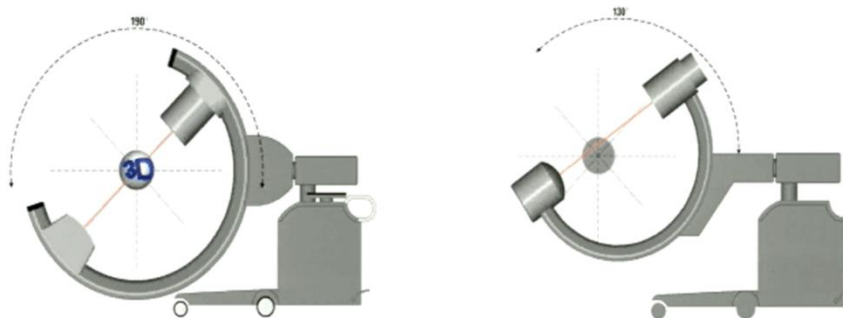
Figure 3. 21 (Left) Isocentric vertical tilt movement. (Right) Not isocentric vertical tilt movement.

The vertical tilt movement is not-isocentric and cannot be used, since in some projection the sample would be out of the small FOV. For this reason, in this work we will work with the horizontal tilt movement which is isocentric keeping always the sample projected into the same area of the detector.

3.3.2 Detector holder

In order to fix the flat panel to the C-arm, a metallic holder shown Figure 3.22 was used. It is composed by two parts: one side is adjusted to the image intensifier of the C-arm using screws and the other part has industrial velcro to attach it to the flat panel.

Figure 3. 22 Flat panel's holder.(Top left) Part of the holder that is introduced in the C-arm detector. (Top middle) Screws to adapt the holder to the C-arm detector. (Top right) Part of the holder that is attached to the flat panel. (Bottom) Flat panel with the flat panel using the holder.

3.3.3 Data pre-processing

We have developed a function in Matlab to perform the pre-processing of the images obtained from the flat panel, that we called `pre_proc_algorithm`. The images obtained from the detector, with a size of 4320x3556 pixels, are stored in HIS format and they are the inputs of this function. This format presents a 100 bytes header while using uint16 datatype for storage.

We can model the data acquired using the Beer-Lambert law that relates the attenuation of X-rays when they go through a medium

$$N_o = N_i * e^{-\int \mu(x)dx} + N_{dark} \qquad (3.1)$$

where a monoenergetic beam is assumed for simplicity. The term N_i is the mean detector signal in the unattenuated beam, and N_o is the raw projection. N_{dark} is the detector signal in the absence of radiation and is typically measured as the average of a reasonable number of detector frames acquired without any X-ray exposure.

The process of 3D reconstruction is essentially a numerical method for solving for the attenuation map $\mu(x)$ given a projection data set N_o. We can obtain the integrals of attenuation, correcting at the same time the raw projections to account for the spatially varying non-uniformities and the detector dark current with:

$$\int \mu(x)dx = -\ln\left(\frac{N_0 - N_{dark}}{N_i}\right) \quad (3.2)$$

We could measure N_i as the mean projection image under irradiation without an object in the field, known a flood-field N_{flood}. The flood-field correction attempts to normalize non-uniform response to the X-ray beam. These data are related to N_i by the following expression:

$$N_{flood} = N_i * e^{-\int 0 dx} + N_{dark} \quad (3.3)$$

By substituting the value of N_i of equation (3.3) into equation (3.2), the value of the integral of linear attenuation is obtained from the intensity of collection according to the expression:

$$\int \mu(x)dx = -\ln\left(\frac{N_o - N_{dark}}{N_{flood} - N_{dark}}\right) \quad (3.4)$$

In Figure 3.23 we can see the intermediate images generated at different stages of the process of generation of X-ray image in the detector.
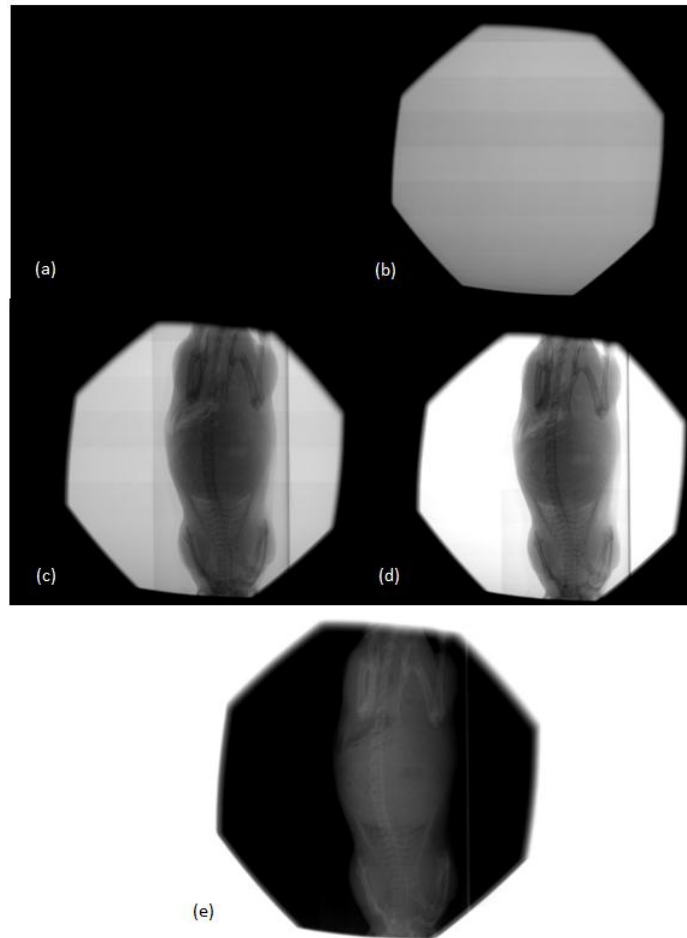
Figure 3. 23 (a) Raw data from detector (No), (b) Flood image (N_{flood}) ,(c)Dark current image (N_{dark}), (d) Corrected transmission, (e) Attenuation image.

The resulting attenuation image is obtained from equation (3.4) and will be input data for the reconstruction software. The final step is to convert these images into a format compatible with Mangoose, the reconstruction software we are using for this work.

Finally, two more image processing steps were added. One of the problems we encountered was the low contrast resolution and the presence of noise, as can be seen in Figure 3.24 In order to improve the quality of the obtained image, processing techniques were applied.
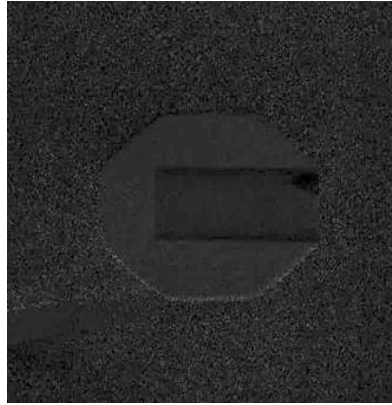
Figure 3. 24 Image before processing techniques.

On one hand, in order to remove noise a smoothing filter was used. Noise reduction can be accomplished by smoothing. Among the different filters that can be implemented, the Gaussian filter was chosen. It has a bell-shaped profile, with a high value element in the center and symmetrical tapering to either side. It produces a response somewhat similar to the average mask, which consist of the average of the pixels contained in the neighborhood of the filter mask, but with even less ringing because of the gradual tapering of its profile [11][12]. The mask elements are given by

$$h(i,j) = Ae^{[(-1/2)*\left(\frac{d}{\sigma}\right)^2]}$$

where A is a scaling factor, d is the distance of a pixel from the center of the mask $(d = \sqrt{x^2 + y^2})$ and σ determines the width of the mask (Figure 3.25). The rule of thumb is to set σ = (2w + 1)/2, where *w* is the size of the feature to be blurred out.
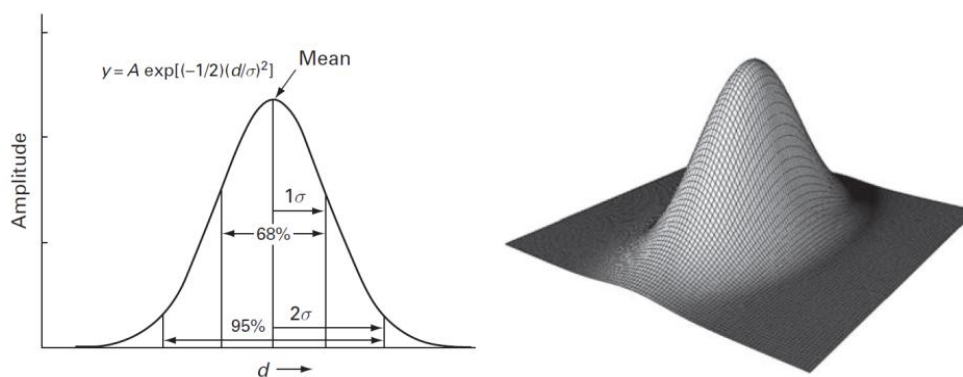
Figure 3. 25 (Left) Gaussian profile (one-dimensional). (Right) wireframe image of a two-dimensional.

On the other hand, the useful area of the detector is reduced to the octagon shown in Figure 3.20 due to a collimator that the C-arm contains, which does not allow us to use the whole surface of the detector. Therefore, to eliminate this non-useful area, each image is multiplied by a circular mask (Figure 3.26).
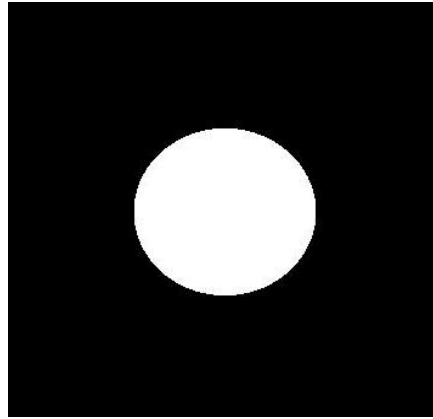
Figure 3. 26 Circular mask.

The result of applying the reconstructed technique is show in Figure 3.27.
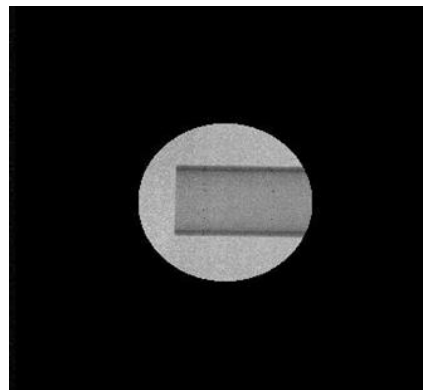
Figure 3. 27 Image after filtering and masking.

4. GEOMETRICAL CALIBRATION

4.1 Calibration algorithm

An important source of artifacts in a tomography system is mechanical misplacements (misalignments) from the ideal positions of both source and detector, resulting from the tolerances in the manufacturing process. Additionally, in the specific case of the system under study, mechanical flex suffered by the C-arm in different positions caused by the heavy loads at its ends can make the geometry parameters further differ from the nominal values [13]. The misalignments that might be present in the system are, on one hand, those related to the detector including inclinations out of the detector plane (roll and tilt), rotation (skew) and translation in X and Y of the panel detector, shown in Figure 4.1.
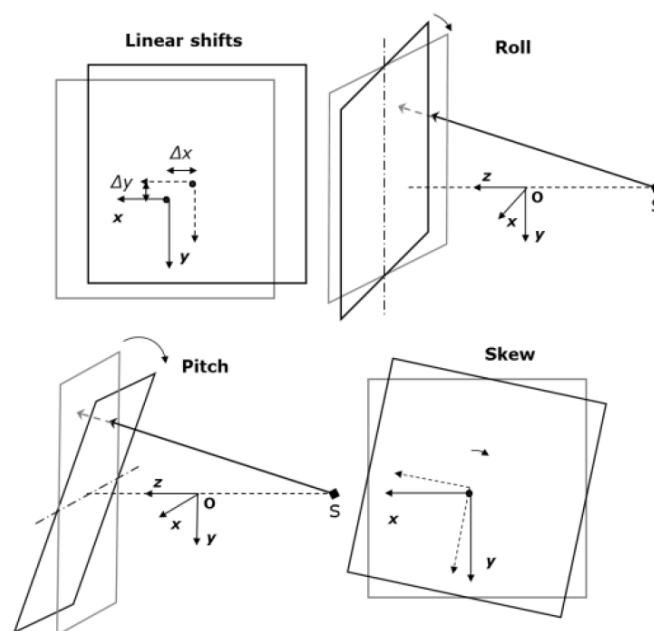
Figure 4. 1 Scheme of the mechanical misalignments in the detector panel.

The objective of the geometrical calibration is to characterize the misalignments of the system in order to obtain an accurate image reconstruction from the projection data. To this end we adapted a calibration algorithm previously developed in the laboratory using Matlab. The parameters are estimated following the Cho's method [14] which was specifically designed to obtain the calibration parameters individually for each

projection. The method uses the projection of a calibration phantom [15] with two circular patterns formed by eight ball bearings symmetrically located in a cylinder.
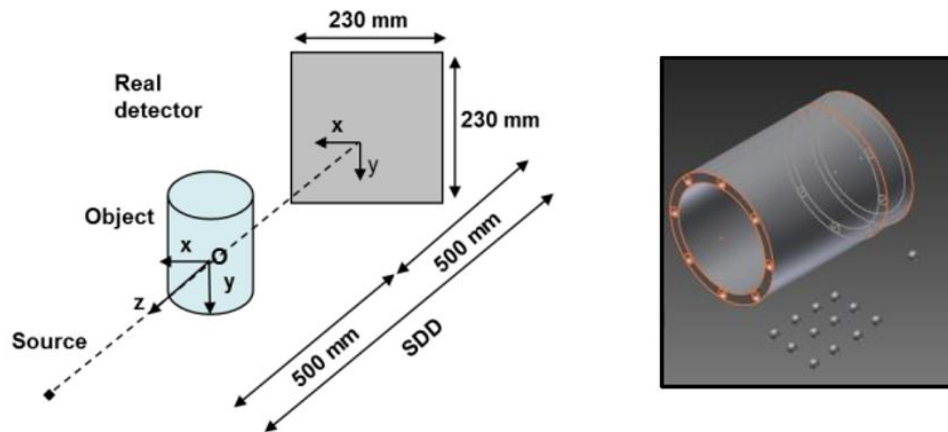
Figure 4. 2 (Left) Scheme of the geometry of the system and (Right) design of the calibration phantom.

For each projection the calibration algorithm follows four steps:

1) Once projections of the calibration phantom have been acquired, the program segments the balls. Figure 4.3 shows an example of a projection before and after segmentation.
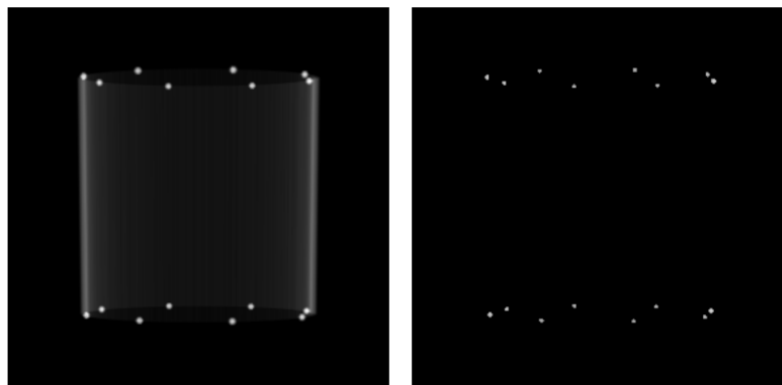
Figure 4. 3 Example of a simulated projection with no misalignment included (right) and result of the segmentation (left).

2) A numerical optimization function in *Matlab* is used to find the center of mass of each ball bearing.

3) The algorithm finds the two ellipses form by the projection of the balls fitting an ellipse to the previously found coordinates of the center of mass of each ball.
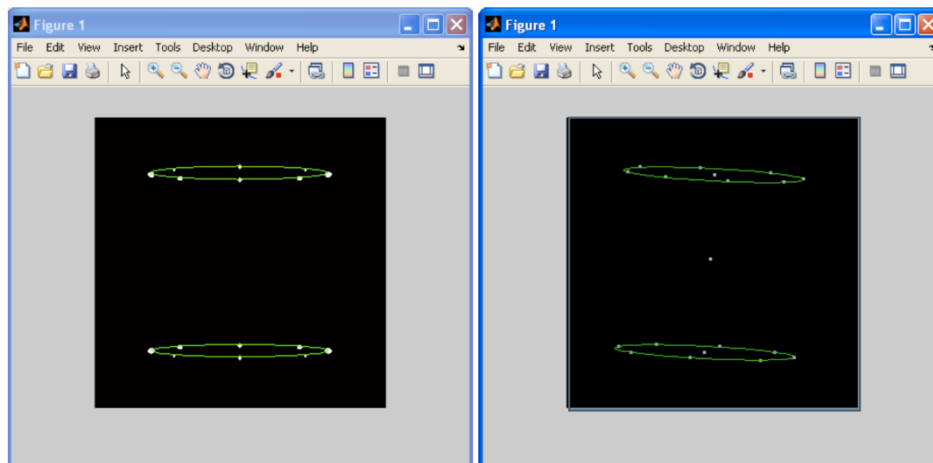
Figure 4. 4 Examples of simulated projections. Adjusted ellipse is displayed on both images with (left) and without (right) rotation.

4) Finally, the algorithm finds out the system parameters based on geometrical relationships between the fitted ellipses, using parameters such as magnitude of major and minor axis and rotation value to find the relative positions of the detector and the source [16].

The resulting mechanical calibration parameters are the following: detector rotation (skew), inclination angles (pitch and roll), piercing point location (projection of the center of the calibration phantom), SDD (source to detector distance) and source and detector position.

These parameters are stored in a calibration file, as can be seen in Figure 4.5.


```
datos_calibracion.txt - Notepad
File  Edit  Format  View  Help
Proj      DSO      DDO       UOffset  VOffset  Pivot    dTeta

0.000    269.869  160.109  159.947  -83.385  -0.005   -1.424
6.000    243.434  143.331  162.163  -72.618   0.291   -1.478
12.000   220.233  128.669  162.988  -65.130   0.662   -1.565
18.000   200.246  116.116  162.466  -60.658   1.106   -1.676
24.000   183.459  105.662  160.653  -59.516   1.628   -1.838
30.000   169.860   97.302  157.609  -62.483   2.211   -1.946
36.000   159.443   91.034  153.292  -63.819   2.817   -1.893
42.000   152.205   86.857  147.608  -64.440   3.441   -1.773
48.000   148.145   84.770  140.640  -61.747   4.101   -1.805
54.000   147.260   84.773  131.204  -54.634   4.814   -1.937
60.000   149.535   86.855  119.464  -43.060   5.590   -2.104
66.000   154.930   90.994  107.839  -29.652   6.384   -2.357
72.000   163.353   97.135   97.873  -16.635   7.102   -2.519
78.000   174.605  105.167   89.507   -7.501   7.748   -2.612
84.000   188.294  114.872   81.246   -1.103   8.343   -2.641
90.000   203.952  126.040   70.038    3.530   8.925   -2.586
96.000   208.651  128.650   57.338    6.325   9.485   -2.432
102.000  203.810  125.583   42.070    7.257   9.996   -1.756
108.000  209.260  129.801   24.657    9.220  10.441   -2.628
114.000  218.028  136.231    7.035    9.615  10.814   -2.419
120.000  228.463  143.886   -8.657    9.182  11.116   -2.142
126.000  240.481  152.792  -22.573    9.356  11.356   -2.702
132.000  252.638  161.844  -32.053    9.389  11.542   -2.632
138.000  259.749  167.098  -33.456    8.745  11.696   -2.276
144.000  257.692  165.726  -29.647    7.508  11.819   -3.372
150.000  249.520  160.120  -27.637    5.775  11.888   -2.432
156.000  239.836  153.477  -29.263    4.156  11.860   -1.679
162.000  230.622  147.146  -38.182    3.296  11.743   -1.009
168.000  222.563  141.651  -48.486    2.868  11.574   -0.419
```

Figure 4. 5 Calibration file.

52

4.2 Calibration phantom

The phantom used to calibrate the C-arm consists of two rings formed by ball bearings mounted on a cylinder in order to be symmetric between them. This phantom has been sized to cover most of the detector field of view (11.5 cm of diameter) provided by the imaging system.

The diameter of each ball bearing was chosen to be large enough to include a large number of pixels, but small enough to minimize overlapping with neighboring balls in projections. The phantom used is a methacrylate tube of 4 mm thick with 16 cavities drilled on each end of the tube. Eight balls are spaced evenly at 45º in two plane-parallel circles separated by 35 mm along the cylindrical tube. The diameter of each ball bearing is 4.7 mm, the diameter of each circular pattern is 46.1 mm. The positions of the balls in both circles are symmetric with respect to the central section plane. The phantom is shown in Figure 4.6.
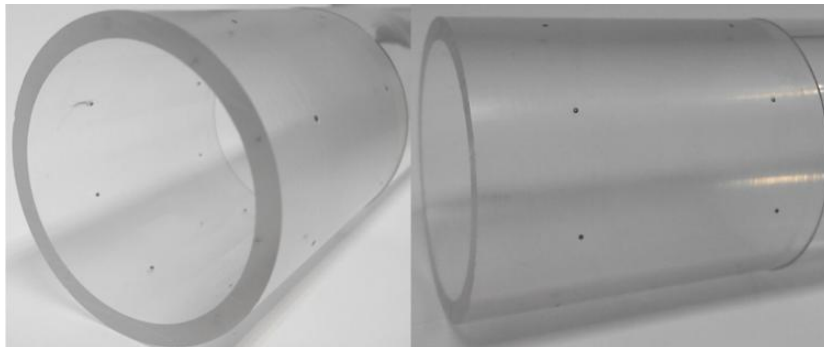
Figure 4. 6 Photograph of the phantom used.

4.3 Preliminary experiments to adapt the calibration algorithm

With the aim of studying what changes we should do in the calibration algorithm explained above, we took projections at different angular positions around the calibration phantom with the C-arm following the horizontal tilt movement. The angular position was monitored by attaching the angular positioning system to the top of the case of the image intensifier and capturing the exact position for each projection.

The calibration phantom has to be correctly placed in the center of the FOV. The first problem we found was the lack of a bed in the C-arm to support the phantom. The length of the phantom was not enough to be in the center of the FOV and also to be supported by a table in a way that it will not interfere with the movement of the C-arm. To be able to place the phantom in the right place, a plastic tube was attached to one end of the phantom. The final position can be seen in Figure 4.7.

Figure 4. 7 Placement of the phantom in the center of the detector by a plastic tube.

It is important to note that the exact position of the phantom is a key factor in order to get a proper calibration file. To assure this, we obtained projections at 0 and 90 degrees to check that is centered for the whole rotation of the system. Figure 4.8 shows an example of an incorrect placement that will not result in correct calibration parameters.
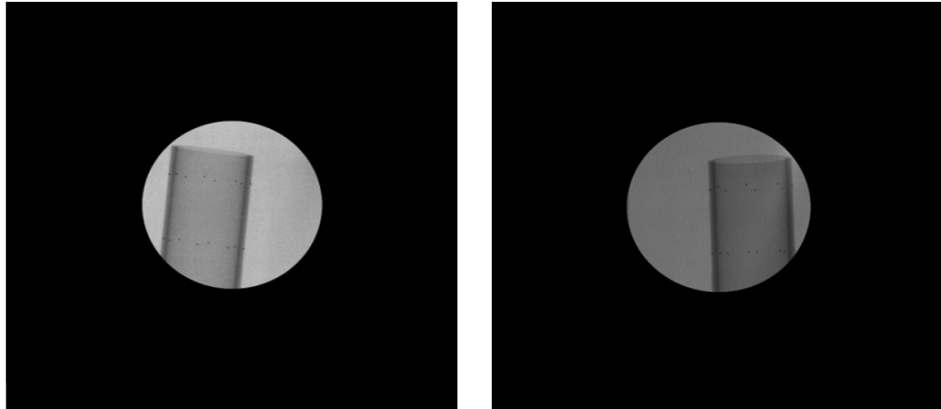
Figure 4. 8 (Left) Projection at 0 degrees. (Right) Projection at 90 degrees.

Figure 4.9 shows a correct positioning of the phantom, where the distance to the center is much smaller than the previous one shown in Figure 4.8.
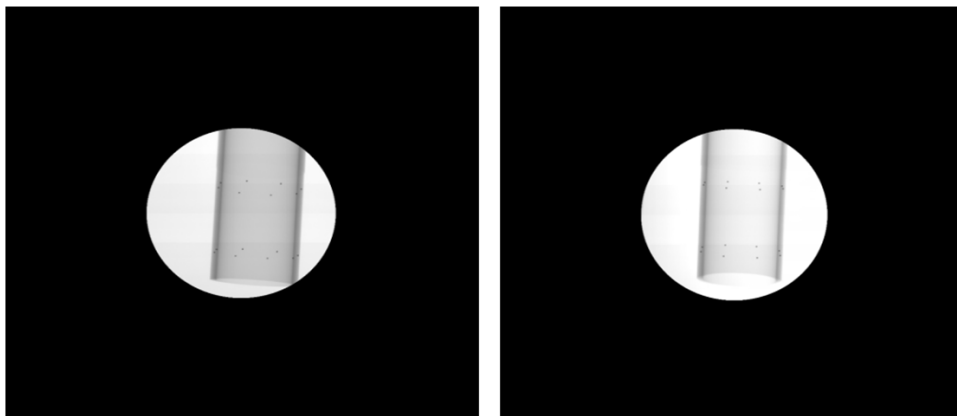
Figure 4. 9 (Left) Projection at 0 degrees. (Right) Projection at 90 degrees.

As explained in section 4.1, the first step is the segmentation of the balls using a threshold introduced by the user that isolates them from the background. Obtaining the proper coordinates of each ball bearing projection allows us to use them in the calibration method, directly or by identifying the ellipse formed by the whole set of ball projections, shown in Figure 4.10.
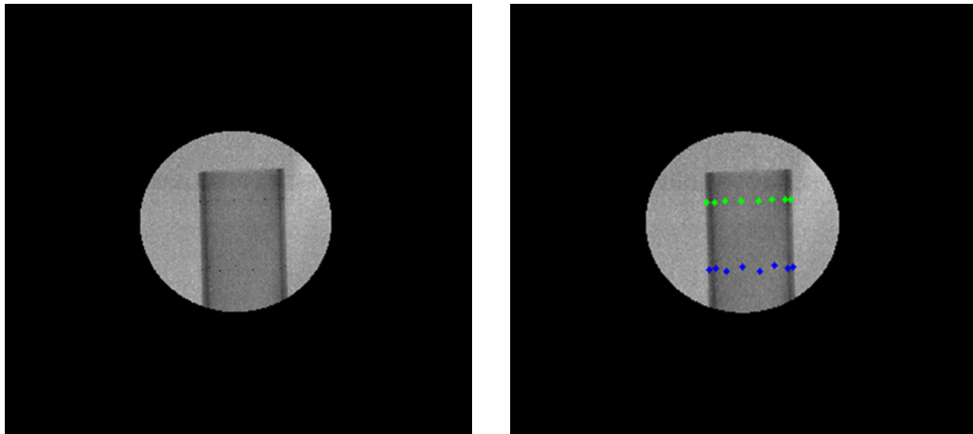
Figure 4. 10 (Left) Input projection. (Right) Segmented ball. Each color corresponds with an ellipse.

However, many of the projections obtained had an artifacts, hindering the detection of the balls, as can be seen in Figure 4.11. This imposed a manual segmentation of these images indicating the position of each ball.
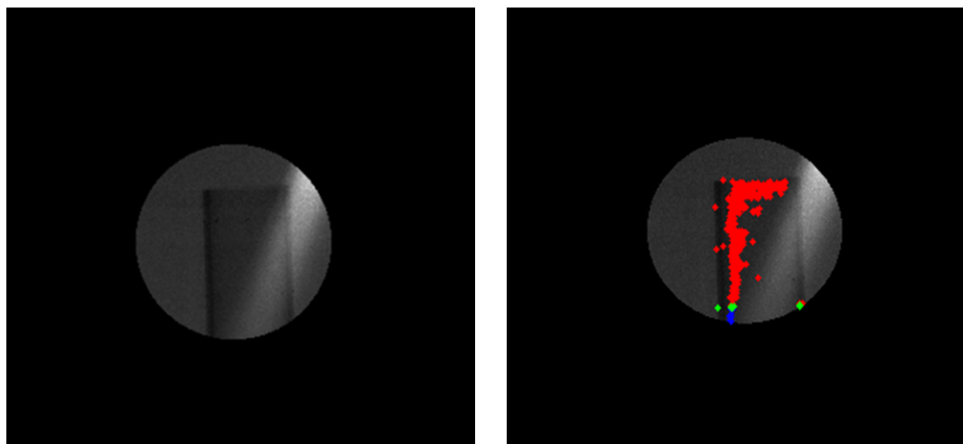
Figure 4. 11 (Left) Input projection. (Right) Error in balls segmentation.

Nevertheless, some of the projections still had to be discarded because it was not possible to detect the exact position of the balls as is shown in Figure 4.12.

Hospital General Universitario
Gregorio Marañón
Comunidad de Madrid
SaludMadrid

Universidad
Carlos III de Madrid
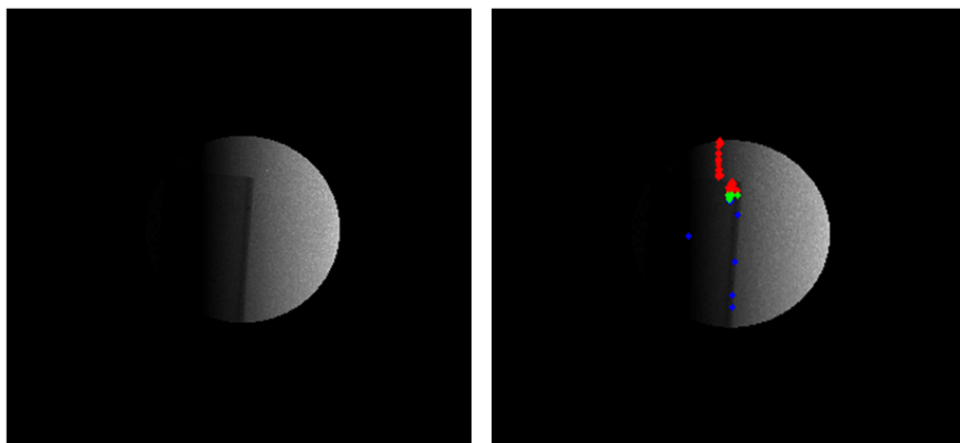
Figure 4. 12 (Left) Input projection. (Right) Error in balls segmentation.

To solve all these problems, we optimized the acquisition parameters (voltage and the intensity of the X-ray source) to find the values that lead to a highest contrast in the projection in order to facilitate the segmentation of the balls. Figure 4.13 show some of the results obtained (zoom-in of the original images). The best results were obtained with a voltage of 92 keV and an intensity value of 3.6 mAs.

Figure 4. 13 Projection image of the calibration phantom obtained with a voltage of 110 keV and an intensity of 3mAs (left), a voltage of 92 keV and an intensity value of 3,6 mAs (middle) and with a voltage of 79 keV and an intensity value (right) of 4.2 mAs.

However, despite using these selected acquisition parameters for all projections, different intensity values were obtained depending on the projection as shown in Figure 4.14 (zoom-in of the original images), probably due to variations of the X-ray source flux.
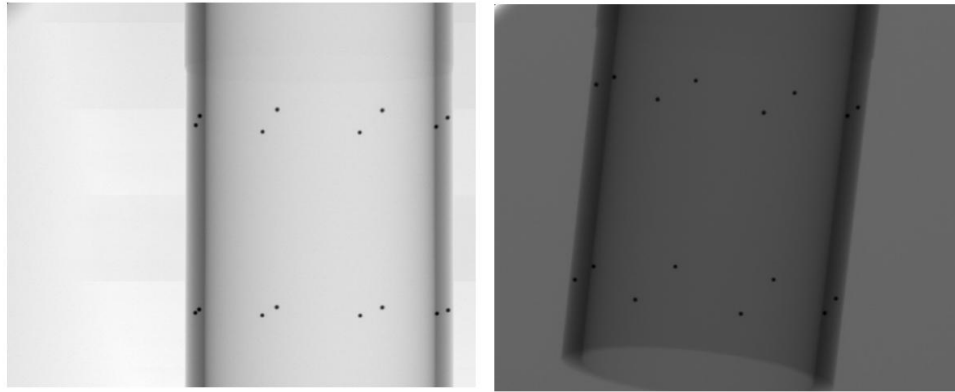
Figure 4. 14 Example of projection with different intensities values.

With the available calibration algorithm a threshold must be introduced by the user at the beginning. Nevertheless, since each image has a different intensity threshold, it had to be changed for each projection which resulted on an increase of user interaction and much longer processing times.

To avoid this problem, we modified the algorithm including a bottom-hat transformation, which is a morphological operation that extracts small elements. These details must be smaller than a structuring element and darker than the surrounding. Therefore, choosing a circular structuring element with a radio of size 4 pixels, the resulting image will show only the balls as can be seen in Figure 4.15
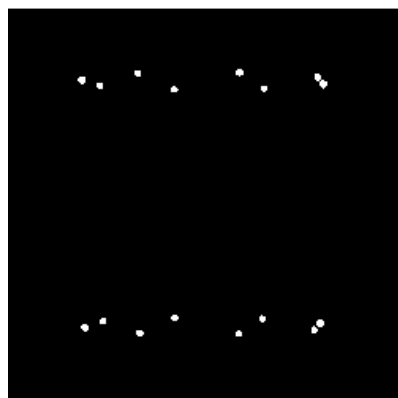
Figure 4. 15 Resulting image after applying bottom-hat transformation.

This result does not depend on the intensity value of the input image and with a unique threshold every balls of each image can be segmented (Figure 4.16).
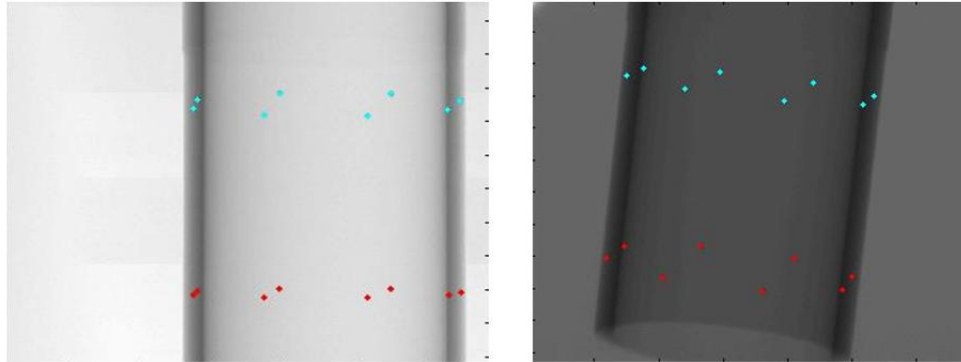
Figure 4. 16 Segmentation of the balls with the same threshold although each image has a different intensity value.

4.4 Calibration process

In order to calibrate the system, we have to follow six different steps shown in the workflow:
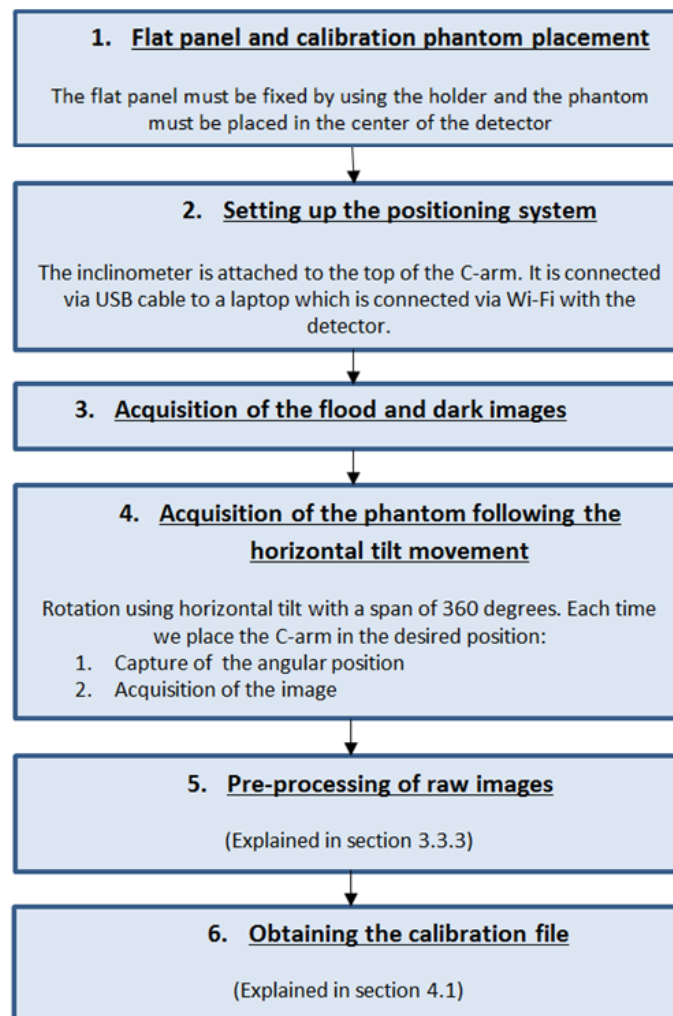
Figure 4. 17 Workflow of the calibration process.

4.5 Results

Figure 4.18 and Figure 4.19 show the values obtained from experiment 2.
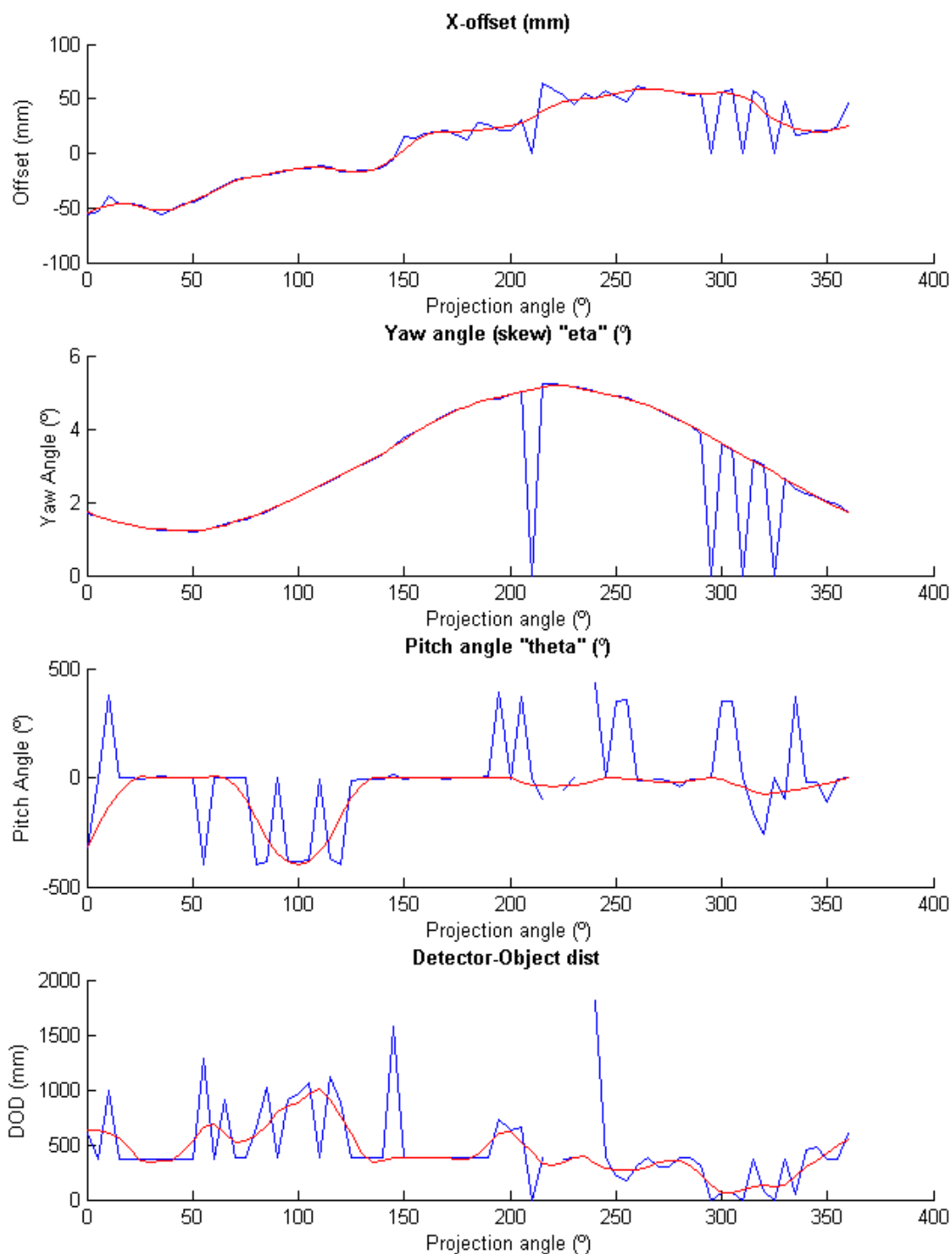
Figure 4. 18 Calibration parameters. Blue line: Raw data. Red line: Smoothed data.
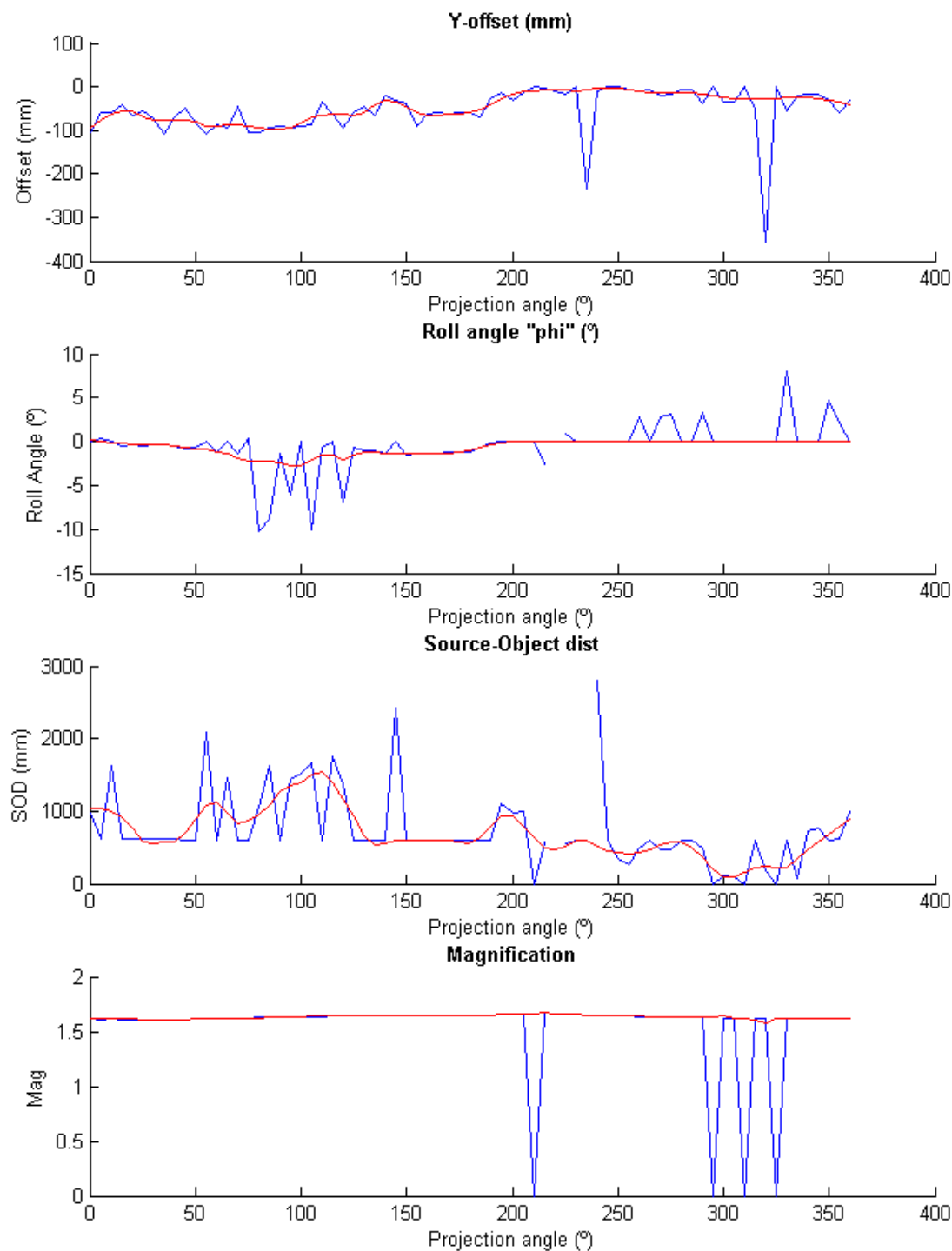
Figure 4. 19 Calibration parameters. Blue line: Raw data. Red line: Smoothed data.

The blue line corresponds to the raw data, which presents several abrupt changes at given angular positions. As the phantom was acquired in a progressive way, the expected data must not contain abrupt changes. One of the causes of these errors is that in some projections several balls may overlap, leading to the wrong calculation of

the ellipses calibration parameters. For this reason, the measurements that do not follow the trend of the rest of the values should be discarded. In order to solve this, we obtained the final set of parameters by smoothing the raw data, resulting in the red curve shown in the plots. Figure 4.20 shows examples of ellipses wrongly calculated, where the blue and red stars set the vertices of each ellipse.
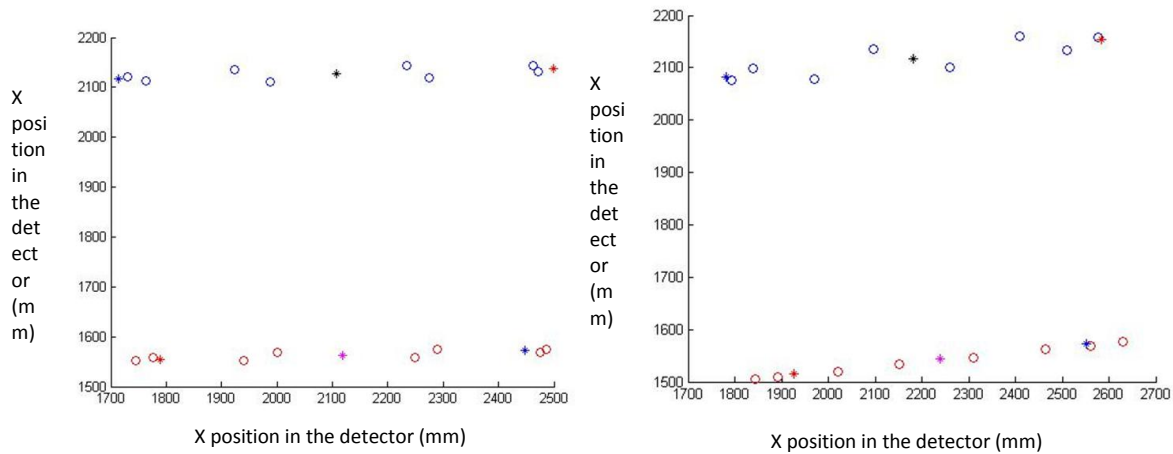
Figure 4. 20 Example of errors in the calculation of the ellipses. Starts show the limits of the axes of the ellipse.

4.6   Repeatability

After obtaining the calibration file, it should be possible to reconstruct other samples if they are acquired in the same angular positions, given that the calibration parameters are constant and invariable in time. We have evaluated the stability of these parameters repeating three times the calibration process. A first calibration was done with 60 acquisitions starting from 0 degrees and with a step angle of 6 degrees. A second calibration was done maintaining the same step angle but starting from 3 degrees. Finally, both acquisitions were combined to get a step angle of 3 degrees.

Figures 4.21 and 4.22 show the calibration parameters obtained for the three experiments.
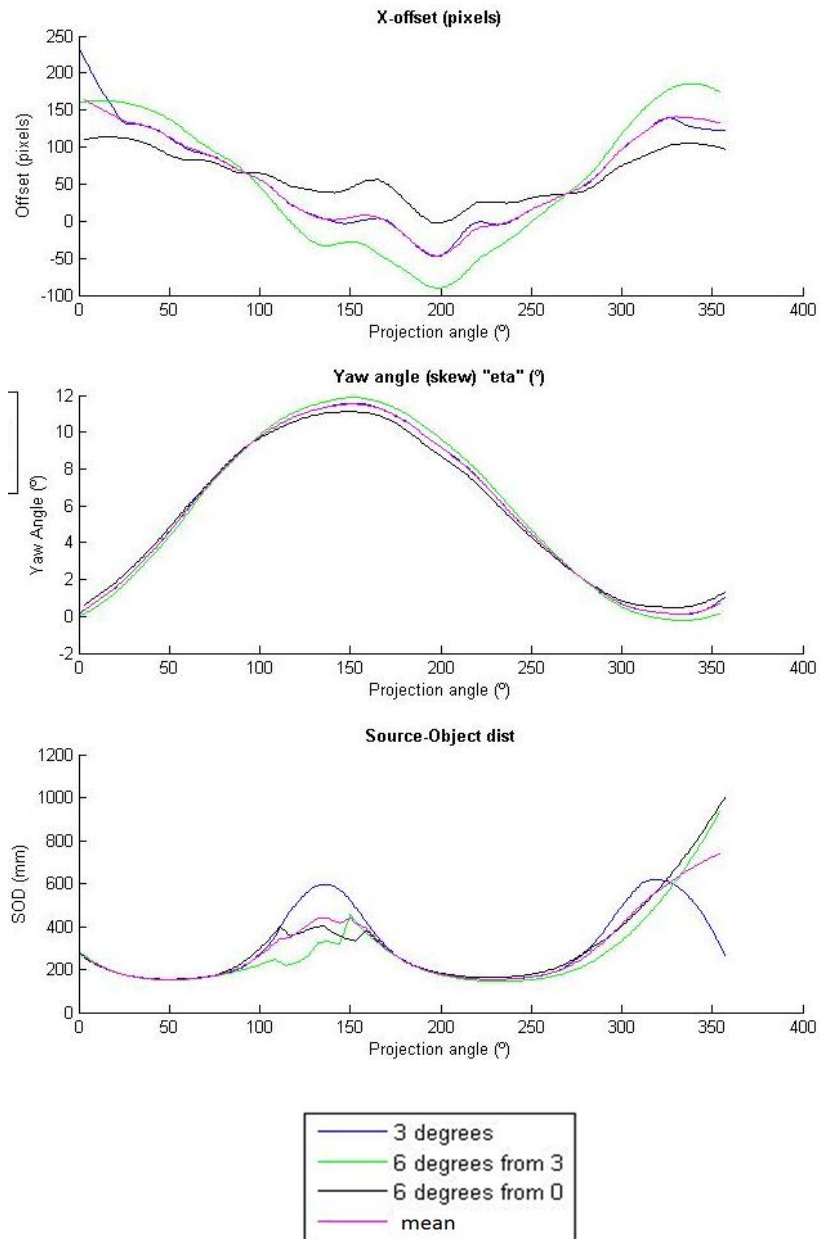
Figure 4. 21 Calibration parameters for different experiments but maintaining the detector in the same position.
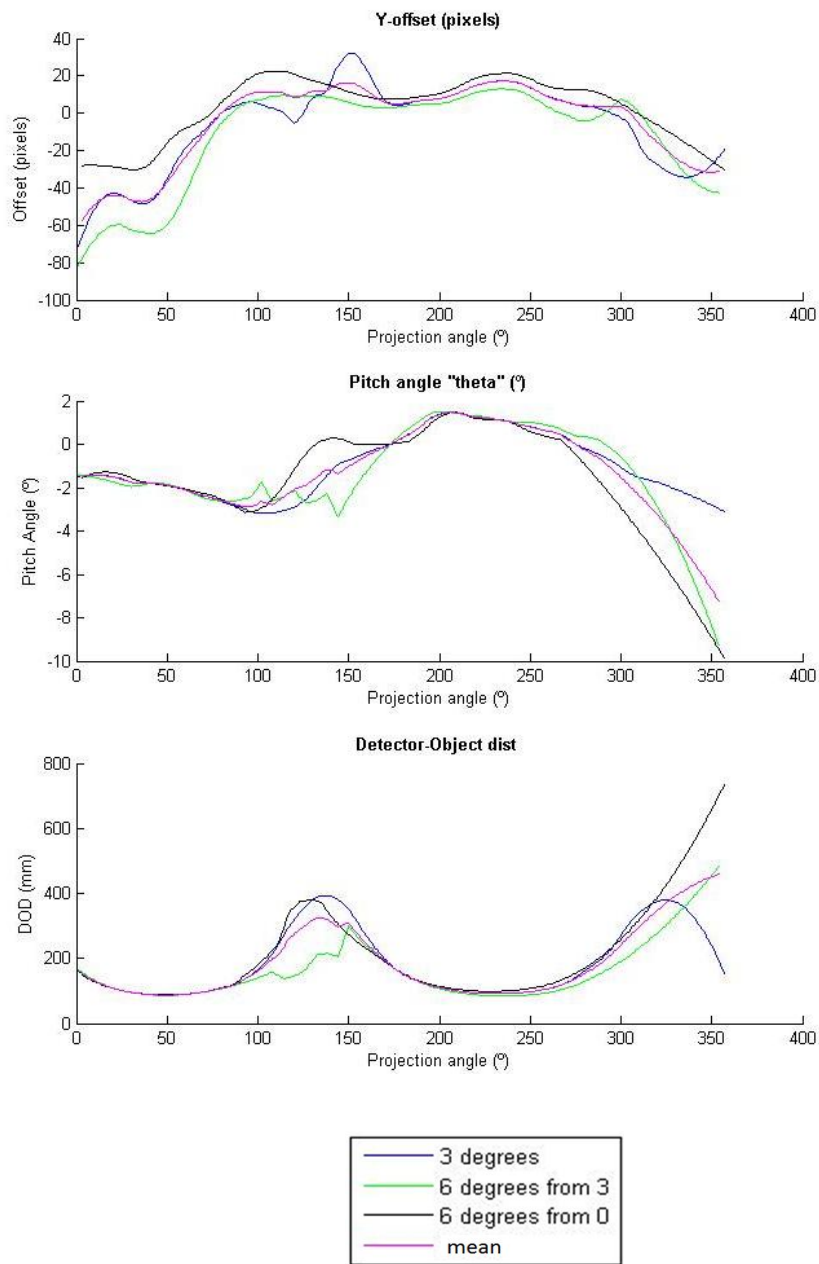
Figure 4. 22 Calibration parameters for different experiments but maintaining the detector in the same position.

As it can be seen in these graphs, the calibration parameters change each time the experiment is repeated. The main origin of this problem is the mechanical strain of the arm mainly due to the heavy holder manufactured for the flat panel detector as can be seen in Figure 4.23. Left panel shows how marks we placed on both sides to investigate this were aligned at the beginning of the experiments. After several projections those marks have a misalignment showing that the vertical position was not the same (Figure 4.23, right).
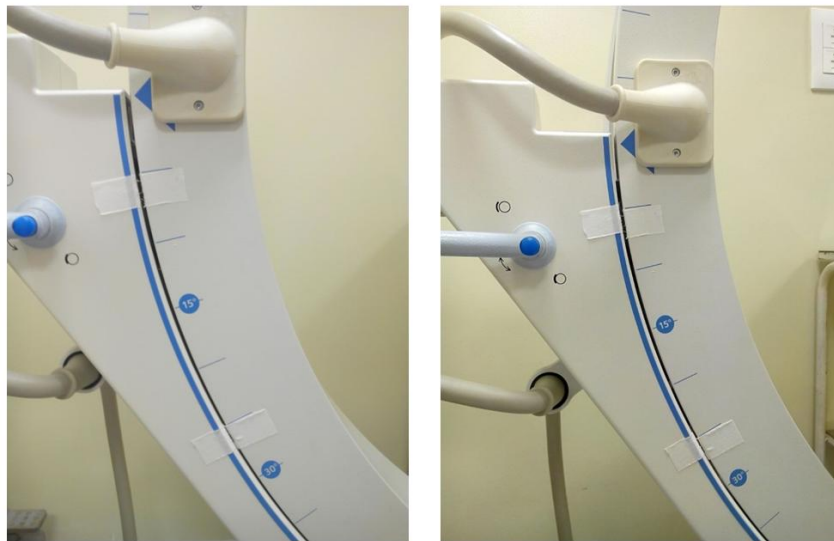
Figure 4. 23 (Left) Marks at the beginning of the experiments. (Right) Marks after some projections.

5. RECONSTRUCTION

The data reconstruction is carried out using `Mangoose`, a reconstruction software based on the FDK method implemented in CUDA language and accelerated thanks to parallel processing in Graphic Processing Units (GPUs). Each projection image must be stored as raw data (data type: float) in a separate file with the name "0n.ct" where n is the projection position in a folder called *subvolume00* together with the calibration file. The description of the rest of the input parameters is shown in Figure 5.1.

-v: voltage of the source (KVp)(float)

-n: number of files (int)

-p: number of projections per file (int)

-b: number of bed positions (int)

-g: binning in the projection (int)

-d: number of pixels that has each projection {proj_dim_s proj_dim_z) (int)

-a: total number of projections (angular positions) (int)

-j: binning in the reconstruction {bin_reco_x bin_reco_y bin_reco_z}(int)

-r: dimensions of the ROI (Region of Interest) in each axis

-i: initial angle (int)

-t: direction of rotation: "-1" or "0" Counter-Clockwise; "1" Clockwise

-k: output data type: "0" unsigned short int; "1" float

-l: to do the logarithm: "1" yes

-#: input data type: "0" unsigned short int; "1" float; "2" signed short int

-uu: name of the calibration file (string)

Figure 5. 1 Description of the input parameters.

The program can be run in Windows from a MS-DOS shell as shown in the following example:
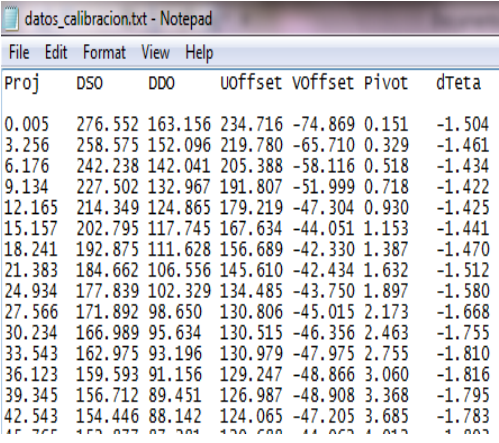
```
Projection size: 678 4720
^C
Z:\agarcia\MangooseSuperArgus_v1.0_binario\Release_CPU>FDK_recon -h ./ -f Z:\aga
rcia\imageCT\ -n 72 -p 1 -g 1 -d 4320 3556 -a 72 -j 1 1 1 -i 0 -t 1 -# 1 -uu dat
os_calibracion -v 45.000 -k 1 -b 1 -l 1 -r 500 500 50
```

Figure 5. 2 Example of Mangoose call.

To have all the data in the right format for `Mangoose`, we need to perform two steps. First we need to combine the file obtained by the calibration algorithm and the angular position file that we have created using the user interface from the values provided by the inclinometer, with a new program created in Matlab called `generate_cal_file`. An example of this final calibration file can be seen in Figure 5.3.

Figure 5. 3 Example of final calibration file.

Second, we need to process the raw data in a .his format captured by the flat panel using the software tool `pre_proc_algorithm` explained in Section 3.3.3.

The reconstruction software generates several files that are stored in the folder where the executable file, `Mangoose`, is located.

- *log_file_z1*: It contains the software call and the details of the different stages of the reconstruction.
- *Progress-ct_z1.list:* it contains a number (1-100) that shows the percentage indicating how much the reconstruction process is completed (100 means that the reconstruction has been finished). If there is an error, the value will be -1 and a file called *error_ct_z1* is generated.
- *Error_ct_z1:* it contains an error message.

Together with these files, the reconstructed volume is stored as raw data (data type: float) in a file with the name "reconstruction_ct0_dimx_dimy_dimz.img" where *dimx*,

dimy, and *dimz* are integers indicating the number of pixels for dimensions *x*, *y*, and *z* respectively.

The results obtained with 60 projections, a span angle of 360 degrees and a step angle of 6 degrees starting in 0 degrees are show in Figure 5.4. Left panel shows the reconstructed image without using the calibration file whereas right panel shows the reconstructed one when the calibration file is applied.
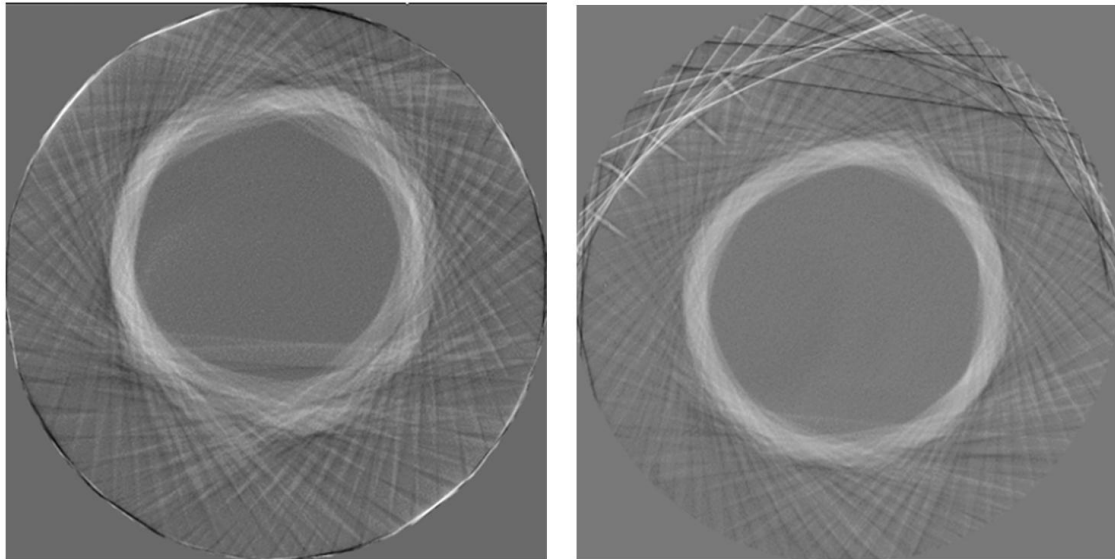
Figure 5. 4 Axial view of the reconstructed image without calibration (left) and with calibration (right).

As explained in Section 4.6, we performed a second acquisition of the same phantom tatking projections with an step angle of 6 starting at 3 degrees. We tried to obtain a reconstructed image putting together both calibrations files in only one calibration file in order to get a step angle of 3 degrees. Figure 5.5 shows an axial view of the reconstructed image, where we can clearly see how the phantom has been reconstructed in two different positions. This is due to poor C-arm stability explained in Section 4.6 that induces changes in the calibration paramters between consecutive studies.
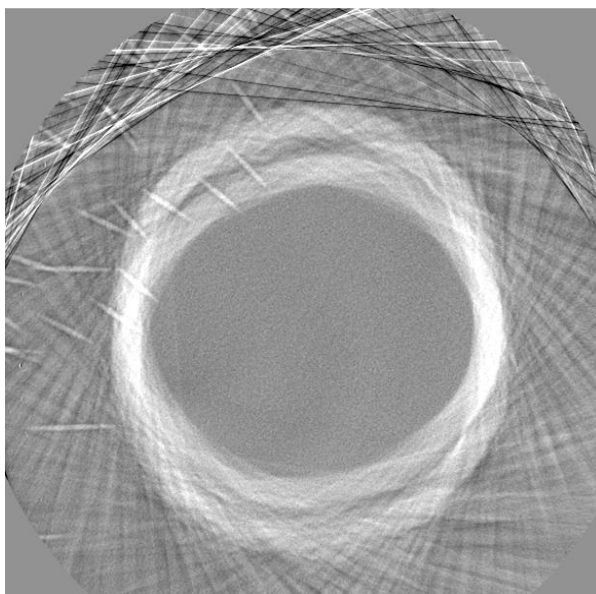
Figure 5. 5 Reconstructed phantom when two calibration file have been put together.

To solve this problem we have reconstructed both files separately and then we have registered both images. Image registration is the process of aligning two or more images of the same scene taken at different times, from different viewpoints, and/or by different sensors so that the corresponding features can easily be related. Figure 5.6 shows the result obtained, where the previous problem has been solved.
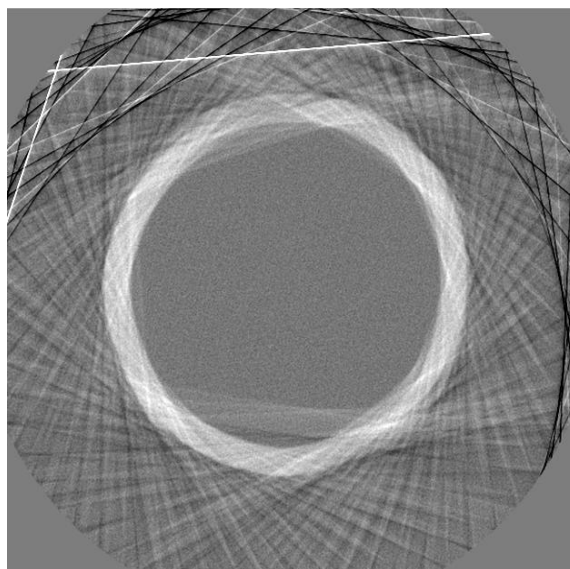
Figure 5. 6 Reconstructed phantom after registration.

6. EVALUATION ON SMALL ANIMAL

Once we have the calibration file obtained by using the calibration phantom, we can obtain the tomography of a different sample as long as the X-ray projection images are acquired at the same angular positions than those stored in the calibration file.

To evaluate the proposed acquisition-reconstruction protocol, a rat was acquired with a step angle of 6 degrees starting from angular position 0 degrees and with a span angle of 360 degrees. In order to place the animal in the center of the detector, a bed from a SPECT scanner was attached to a table as shown in Figure 6.1.
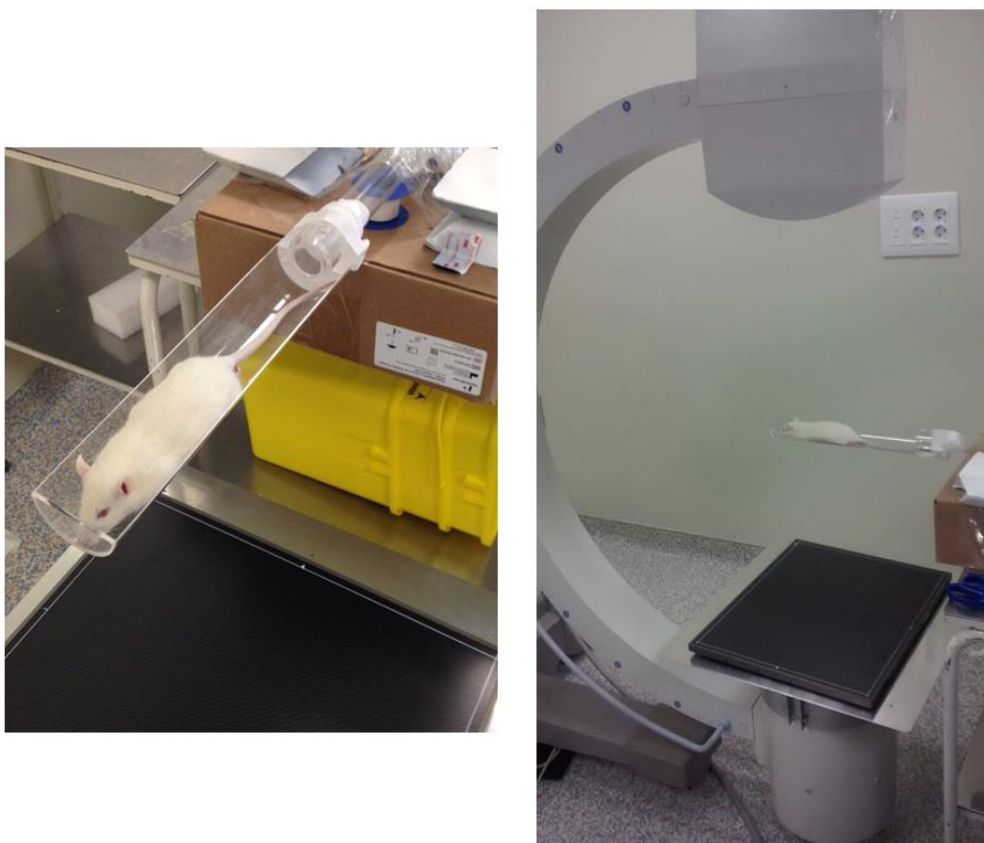
Figure 6. 1 *Placement of the small animal.*

The acquisition parameters were the same as those from the calibration study: voltage of 92 keV and intensity of 3,6 mAs. Therefore, acquiring at the same position than the position stored in the calibration file, 60 projections was obtained. Two of these projections are shown in Figure 6.2.
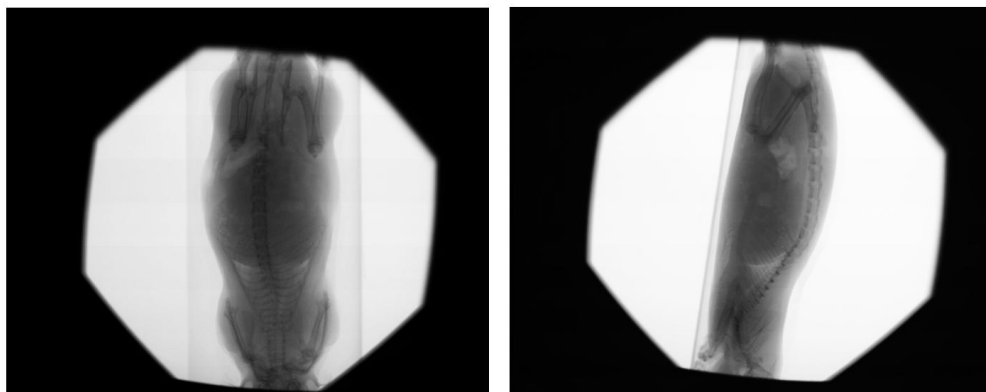
Figure 6. 2 Example of the projection obtained. (Left) Projection at 0 degrees. (Right) Projection at 90 degrees.

These raw images were processed using the developed software tool `pre_proc_algorithm` explained in Section 3.3.3 carry out the flood-dark correction and obtain the attenuation image in the right format for reconstruction. These pre-processed images together with the calibration file were given as input parameters to `Mangoose` to obtain the reconstructed image. The result was a volume with a matrix size of 1000x1000x1000 and voxel size of 0.1 mm. Figure 6.3 shows an axial view of the abdomen, with and without calibration. As can be seen in these results, misalignment artifacts severely affect the quality of the image making the calibration very important step.
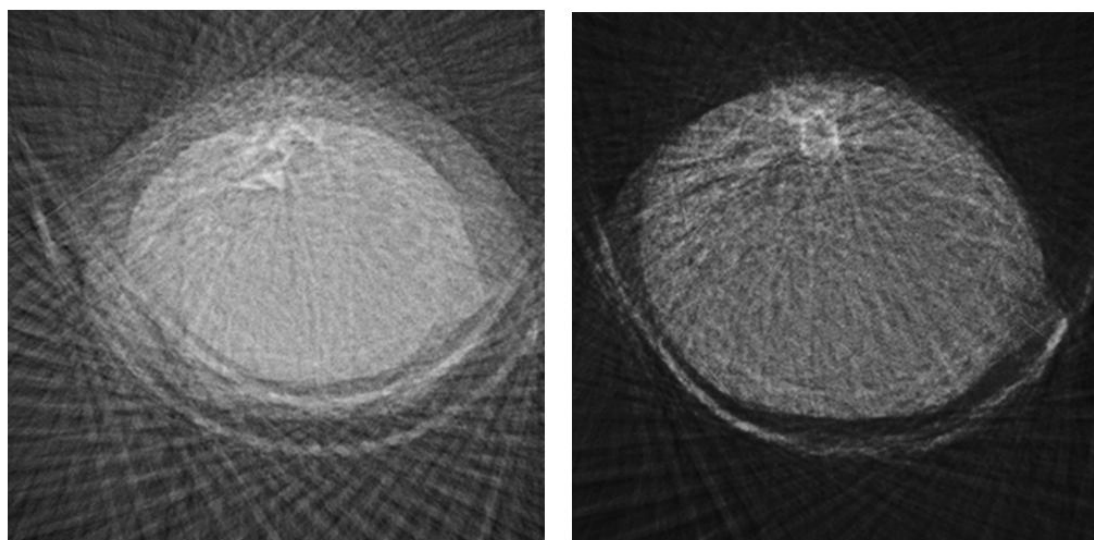
Figure 6. 3 Axial view of the abdomen (Left) Reconstructed image without calibration. (Right) Reconstructed image with calibration.

7. DISCUSSION AND CONCLUSION

This thesis has focused on incorporating tomography capabilities in a system originally designed for planar images: the SIREMOBIL C-arm developed by SIEMENS. As a result we have designed a new acquisition protocol that solves the effects of the non-idealities that hinder its use as a tomograph, including an exhaustive calibration of the system, not needed when it is used for planar imaging.

First of all, we have shown using simulations that even small errors in the projection angle estimation lead to artifacts in the reconstructed image, indicating the need of a positioning system to obtain higher accuracy than the one provided by the simple calibration included in the system. We have developed a positioning system based on the ADIS16209 digital inclinometer connected to the computer by a single board microcontroller (LaunchPad board). The system is controlled through a user interface developed using the software package Processing and gives as a result a text file with the exact angular positions. After the proof of concept, the connections between both component (board and inclinometer) were done with a PCB (design using Eagle and manufactured by WEdirekt).

Secondly, the detector included in the C-arm is based on an image intensifier which is an analog detector that presents distortions. These distortions, that are not critical in planar images, may produce severe artifacts in the reconstructed image. To solve this problem, and also, to obtain digital images required to perform the reconstruction, we have integrated a flat panel detector in the C-arm: the XRpad 4336 detector. The dimensions of this detector (35×43 cm) are much bigger than those of the image intensifier integrated in the C-arm (a circle of 23 cm of diameter), which would enable a bigger field of view. However, the system has a built-in collimator to restrict the X-ray beam to the dimensions of the original detector reducing also the useful area of the flat panel. This poses a problem with regard to the type of rotation movement that we can do with the C-arm. The horizontal tilt movement is isocentric keeping always the sample projected into the same area of the detector; however, the vertical tilt movement is not-isocentric and cannot be used, since in several projections the

sample would be out of the small field of view. Eliminating the collimator would allow to increase the field of view from 10 to 22 cm enabling the vertical tilt.

Furthermore, the C-arm has a certain flexibility presenting different mechanical strains depending on its position due to the weight of the source and detector. To obtain an accurate image reconstruction from the projection data we need to carry out a geometrical calibration to characterize the position of the source and detector each time the arc is moved. A calibration has been developed adapting a calibration algorithm based on the work by Cho et al. available in the laboratory. The calibration phantom consists of two rings formed by ball bearings mounted on a cylinder in order to be symmetric between them. The diameter of each ball bearing was chosen to be large enough to include a large number of pixels, but small enough to minimize overlapping with neighboring balls in projections. A study of different acquisition parameters (voltage and the intensity of the X-ray source) was done to find the values that lead to a highest contrast in the projection in order to facilitate the segmentation of the balls, which is based on thresholding. However, since some of the acquired projections had different intensity values (probably due to variations of the source), the threshold had to be changed for each projection which would result on longer processing times. To avoid this problem, we modified the algorithm including a bottom-hat transformation, a morphological operation that extracts small elements independently of the intensity values of the input image.

Reconstruction was done using Mangoose, a reconstruction software available in the laboratory. To this end a post-processing software was developed that combines the calibration parameters with the angular position file and converts the images acquired with the flat panel to the format compatible with Mangoose.

After obtaining the calibration file, it should be possible to reconstruct other samples if they are acquired at the same angular positions, given that the calibration parameters are constant and invariable in time. We have evaluated the stability of these parameters repeating the calibration maintaining the same positions. Nevertheless, the results show that these calibration parameters are different, which is a problem when we want to reconstruct something different from the calibration phantom. The

main reason of this no repeatability of geometrical parameters is a mechanical strain of the C-arm on the other rotation direction due to the weight of the holder for the flat panel.

Finally we have evaluated the proposed protocol on real data, both on a phantom and on a rodent study. The results show the feasibility of the proposal.

Part of this project has been presented as oral communication in the Congreso Anual de la Sociedad Española de Ingeniería Biomédica (CASEIB). As result, a scientific publication has been obtained (de García-Santos et al 2014). Finally, it should be noted that the work of this thesis has a clear application in industry, since it is part of a proof of concept of the new generation of C-arm systems which will be market worldwide by the company SEDECAL.

8. LIMITATIONS AND FUTURE WORK

One of the main problems we have found is that the calibration values vary from one experiment to another. It supposes a limitation if we want to obtain a good quality reconstructed image of a sample different from the calibration phantom. As it is explained in section 4.6, the main reason of this no repeatability of geometrical parameters is a mechanical strain of the C-arm on the other rotation direction due to the weight of the holder for the flat panel. Future work will be the repetition of these experiments with a C-arm with an integrated digital detector.

Other important limitation is the inability to use the vertical tilt movement since it is not isocentric, which is a problem in our case due to the small FOV we have. Given that with the horizontal tilt only the head and the limbs of the patient can be acquired, the evaluation of the vertical tilt movement would be an important breakthrough as it would be able to acquire any part of the body as shown in Figure 8.1.

Figure 8. 1 Acquisition of the abdomen of a patient changing the vertical tilt movement

reconstruction for acquisitions with low number of projections. Future work will include the use of a more advanced reconstruction algorithm, which will increase the quality of the reconstructed images not only from few numbers of projections but also with a smaller span angle.

9. PROJECT MANAGEMENT

In this chapter the global cost of the realization of this project are presented. Personnel cost and material cost are treated separately.

9.1   Planning

The project has been developed following a model structured in six phases that have associated tasks described below. Time assigned to each one of the tasks is estimated in weeks. Each working week corresponds to 20 hours.

1. **Requirement determination phase**

This phase includes the definition of the objectives of the project and the determination of the tasks involved to achieve them.

> Estimated time: 1 week

2. **Angular positioning system phase**

· Study of the effect of errors in the angular positioning.

· Study of a solution.

· Installation of the tools proposed to solve the problem of a poor angular accuracy.

· Initial contact with the programming languages that are needed to program the microprocessor and to create the user interface.

· To carry out a preliminary experiment of both implementation.

· Design of the PCB.

· Publication of the scientific paper.

· Oral communication in the CASEIB in Barcelona.

> Estimated time: 8 weeks

Hospital General Universitario
Gregorio Marañón
Comunidad de Madrid
SaludMadrid

Universidad
Carlos III de Madrid

3. Geometrical calibration phase

·   Adaptation of the flat panel by a metallic holder.

·   Creation of an algorithm in Matlab to adapt the images obtained from the flat panel to a format compatible with the reconstruction software.

·   Study of the calibration algorithm developed previously in the lab.

·   Study of the adaptation of this algorithm to our system.

·   Experiments to adapt the algorithm to the image obtained with our system.

·   Development of an calibration protocol

·   Analysis of the obtained results.

·   Study of the repeatability of the calibration parameters.

> Estimated time: 11 weeks

4. Reconstruction phase

·   Creation of an algorithm in Matlab to obtain the final calibration file.

·   Development of a reconstruction protocol

·   Study of the parameter that are needed to be introduced in the Mangoose software.

·   Study of the reconstructed phantom image.

> Estimated time: 2 weeks

5. Evaluation on small animal

·   Repetition of the calibration procedure using a small animal.

·   Obtaining the reconstructed image following the reconstruction protocol.

·   Study of the result.

> Estimated time: 1 week

6. Project report development phase

In this last phase of the project the report is developed, where all the work done, conclusions and future work are presented.

> Estimated time: 9 weeks

Therefore, total time estimation in hours is 640 hours.

9.2 Estimated budget

9.2.1 Personnel cost

The total personnel cost associated to the development of the project is:

CATEGORY	TIME (HOURS)	COST/HOUR (€)	COST (€)
Biomedical engineer	640	15	9,600.00
Project coordinator	150	35	5,250.00
Research engineer	200	20	4,000.00
		TOTAL	18,850.00

Table 9. 1 Personnel cost breakdown

9.2.2 Material cost

Below the costs of used material in the realization of the project are shown:

9.2.2.1 Inventoriable material

The following table shows the material used in the project with a depreciation of **20% at five years**.

MATERIAL USED	COST(€)	COST/YEAR (€)	DEDICATION	COST (€)
Personal computer. AMD Athlon™64 X2 Dual Core Processor 5200+ 2.60 GHz 4,00 GB RAM	1000	200	8 months	133.00
Matlab programming language license	6000	1200	8 months	800.00
XRpad 4336 detector (PerkinElmer)	35000	7000	50 hours	40.00
C-arm+Operating room	30€/hour		50 hours	1,500.00
			TOTAL	2,473.00

Table 9. 2 Inventoriable material cost breakdown

9.2.2.2 Fungible material

MATERIAL USED	COST (€)
ADIS16209	114.00
TM4C123G	18.00
Printed Circuit Board (PCB)	76.00
Holder	*
Phantom	150.00
Others(connectors, wire…)	10.00
TOTAL	**368.00**

Table 9. 3 Fungible material cost breakdown

* The detector holder was provided by SEDECAL without any cost.

9.2.3 Indirect cost

Indirect costs are calculated to be 20% of the material and human costs, which is 4338,2 €.

9.2.4 General cost and industrial benefit

The general costs and industrial benefit correspond respectively to 16% and 6% of the material costs. Then the general costs are estimated to be 454. 56 € and the industrial benefit 170. 46€.

9.2.5 Total cost

From the obtained result of cost including personnel and material, final budget is calculated taking account the 21% VAT:

CONCEPT	COST (€)
Personnel cost	18,850.00
Total material cost	2,841.00
Indirect cost	4,338.20
Total cost without VAT	26,029.20
VAT (21%)	5,466.13
TOTAL	**31,495.33**

Table 9. 4 Summary of the costs

Therefore, the total budget of this project comes up to:

Total budget: 31,495.33 €

APPENDIX

A. SCIENTIFIC PUBLICATION DERIVED FROM THIS THESIS

A. García-Santos, C. de Molina, I. García, J. Pascau, M. Desco, M. Abella. *Enhancement of the angular calibration accuracy in a C-arm for its use in tomography.*
Congreso Anual de la Sociedad Española de Ingeniería Biomédica (CASEIB), Barcelona, 2014.

Sesión VI/A: **Imágenes Médicas II** (Sala: Auditori)

Moderadores: D. Manuel Desco, Dña. Begoña Acha

Hora	ID	Título	Autores	Afiliaciones
09:15	739	Método de segmentación mejorado para lesiones cutáneas de tipo no melanoma usando Modelos de Contornos Activos	Abbas, Qaiser (1); Fondón, Irene (2); Sarmiento, Auxiliadora (2); Celebi, M. Emre (3); Aguilera, Pablo (2)	(1) Department of Computer Science, COMSATS Inst. of Information Technology, (2) Departamento de Teoría de la Señal, Universidad de Sevilla, Sevilla, España, (3) Department of Computer Science, Louisiana State University, Shreveport, LA, USA
09:30	746	Evaluation of the effect of angular calibration accuracy in a C-arm for its use in tomography	García Santos, Alba (1); de Molina Gómez, Claudia (1); García Barquero, Inés (1); Pascau González-Garzón, Javier (2); Desco Menendez, Manuel (3); Abella García, Mónica (1)	(1) Dept. Bioingeniería e Ingeniería Aeroespacial, Universidad Carlos III de Madrid, (2) Instituto de Investigación Sanitaria Gregorio Marañón, Madrid, (3) Centro de investigación en red en salud mental (CIBERSAM), Madrid
09:45	756	Modelo de Mezcla de Gaussianas Generalizadas para Segmentación de Melanomas	Sarmiento Vega, Auxiliadora (1); Fóndo García, Irene (1); Velasco Montero, María del mar (1); Qaisar, Abbas (2); Aguilera Bonet, Pablo (1)	(1) Departamento de Teoría de la Señal y Comunicaciones. Universidad de Sevilla, España, (2) College of Computer and Information Sciences, Al-Imam Muhammad ibn Saud Islamic University, Arabia Saudi

Sesión VI/B: **Rehabilitación** (Sala: Beta)

Moderadores: D. Entique Gómez, Dña. Maite Mújika

Hora	ID	Título	Autores	Afiliaciones
09:30	772	Ontología del dominio de la neurorehabilitación cognitiva para un sistema de representación del conocimiento implícito en la elaboración de planes terapéuticos.	Caballero Hernández, Ruth (1); Luna Serrano, Marta (1); García Molina, Alberto (3); Tormos Muñoz, José María (3); Gómez Aguilera, Enrique J. (1)	(1) Grupo de Bioingeniería y Telemedicina, ETSI Telecomunicación, Universidad Politécnica de Madrid, Madrid, España, (2) Centro de Investigación Biomédica en Red en Bioingeniería, Biomateriales y Nanomedicina, Madrid, España, (3) Instituto Universitario de Neurorrehabilitación Guttmann-UAB, Barcelona, España
09:45	776	Perfil cognitivo disfuncional de pacientes con daño cerebral adquirido basado en modelos neuropsicológicos y en estudios de imagen médica.	Luna Serrano, Marta (1); Caballero Hernández, Ruth (1); Chausa, Paloma (1); García Molina, Alberto (3); Tormos Muñoz, José María (3); Gómez Aguilera, Enrique J. (1)	(1) Grupo de Bioingeniería y Telemedicina, ETSI Telecomunicación, Universidad Politécnica de Madrid, Madrid, España, (2) Centro de Investigación Biomédica en Red en Bioingeniería, Biomateriales y Nanomedicina, Madrid, España, (3) Instituto Universitario de Neurorrehabilitación Guttmann-UAB, Barcelona, España

Enhancement of the angular calibration accuracy in a C-arm for its use in tomography

A. García-Santos[1], C. de Molina[1,2], I. García[1,2], J. Pascau[1,2], M. Desco[1,2,3], M. Abella[1,2],

[1] Dept. Bioingeniería e Ingeniería Aeroespacial, Universidad Carlos III de Madrid, España
[2] Instituto de Investigación Sanitaria Gregorio Marañón, Madrid
[3] Centro de investigación en red en salud mental (CIBERSAM), Madrid

Abstract

The C-arm radiology equipment offers a wide variety of movements that, together with its characteristic structure, makes it possible to be used in intraoperative scenarios. Such a scanner is conventionally intended to obtain planar images with no depth information. Our group is evaluating the use of the C-arm as imaging guide and support equipment in Intraoperative Radiation Therapy procedures. For its use in Computed Tomography (CT), it is important to have accurate mechanical calibration and angular positioning in order to reduce the artifacts in the reconstructed image. In this work, we show the effects of small errors in the angle position of the C-arm by simulation. In order to obtain this angular position with the required precision for 3D reconstruction, we have implemented a positioning system based on a digital inclinometer and a user interface. It extracts the angle values with a higher accuracy than the C-arm provides (0.1° vs 5°).

Introduction

The goal of Intraoperative Radiation Therapy (IORT) treatments is the irradiation of post-resected tumor beds or partially resected tumors avoiding, as possible, affecting critical organs [1]. The choice of the volume of irradiation and the total dose for the tumor are the basis for planning external radiotherapy, done on CT image. Given the difficulties derived from the change of the anatomy during surgery, the IORT planning is not an obvious task. Our group at Gregorio Marañón Hospital has developed a radiation therapy planning tool [2, 3], but the complete evaluation would need an imaging technique to evaluate the real situation after surgery. This simulator allows the introduction of concepts from external radiotherapy resulting in what is known as Image Guided Radiation Therapy (IGRT). This concept includes the acquisition of 2D and 3D images before, during, and after radiation [4, 5].

The mobile fluoroscopic system is known as C-Arm. It consists of two units: the X-ray generator and the detector (image intensifier or flat panel) mounted in an arc-shaped wheeled base, and the workstation unit used to visualize, store, and manipulate the images. The C-arm allows a great variety of movements, and its characteristic structure makes it possible to be used in intraoperative cases, as the arc can be situated around the patient lying in the bed. It is used to obtain intraoperative planar images in different surgical procedures such as cardiology, orthopedics, and urology.

We propose to use a C-Arm as a tomograph to obtain 3D images of the patient during IORT. In that sense, the C-Arm will work analogously to a CT scanner with cone-beam geometry. The use of a C-arm for tomography presents several difficulties. It may have mechanical strains and looseness in the detector (image intensifier) and the movements of source and detector may differ from a circular path. Moreover, it is necessary to consider the repeatability of the acquisitions for same positions at different moments. To obtain good quality images, it is necessary to evaluate the effects of these non-idealities and to perform an exhaustive calibration of the system, not needed when it is used for planar imaging [6].

In previous works, we presented the effects of the possible misalignments of the image detection panel of the C-Arm [7] and showed the necessity of calibrating this equipment in order to generate 3D images. Other work was focused on the implementation of a calibration method that characterizes the geometry of the system [8]. Besides the mechanical calibration of the source and detector relative positions, it is necessary to obtain the angular position of the system as a whole.

In this work, we present the effects of errors in the angle positioning and describe the implementation of a positioning system that obtains the angular position with the required precision for a tomography reconstruction. Our experiments are based on the C-Arm Model SIREMOBIL Compact L of Siemens.

1. System under study

The SIREMOBIL C-Arm consists of an X-ray source and an image intensifier attached to a C-Arm gantry. The geometry is depicted in Figure 1.
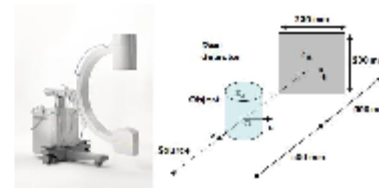

Figure 1. Left: SIEMENS C-Arm. Right: Geometry parameters of the cone-beam system

The C-arm can rotate around two different axes in order to obtain X-ray images of the region of interest from different angular positions. We will refer to the two rotations that the system is able to perform as vertical rotation and horizontal tilt.

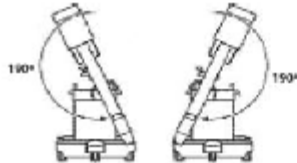- Horizontal tilt is a rotation around the horizontal supporting arm and spans 360° (Figure 2)

Figure 2. Horizontal tilt

- Vertical movement consists on a rotation on the C-arm plane and spans a range from +90° to -40° starting from the neutral position (Figure 3). This position is reached when both the X-ray generator and the detector are aligned in the vertical plane.

Figure 3. Vertical rotation

This system, which is not aimed for tomography, is completely manual and only has a very rudimentary angle positioning: a scale drawn in the arm with a resolution of 5°, as can be seen in Figure 4.

Figure 4. Angular scale in the C-arm's arc.

1. Effects of errors in the angular positioning

With the aim of studying the effects of errors in the angular positioning of the system on the reconstructed image, we have used a simulation tool developed in the group that emulates the functioning of an X-ray system: it produces a set of projections of synthetic phantoms based on the parameters that describe the real system (shown in Figure 1). This tool is implemented in CUDA language and accelerated thanks to parallel processing in Graphic Processing Units (GPUs). Data reconstruction is done with Mangoose, a multi-bed reconstruction software based in the FDK analytical method [9].

We have used a synthetic phantom with similar physical characteristics to human bones and water that fit in the Field Of View (FOV) of the C-arm under study (114.4 mm diameter). It consists of a methacrylate cylinder of 200x100 pixels, 0.8 mm pixel size with two ellipsoidal balls inside of 40 pixels diameter (Figure 5).

Figure 5. Simulated phantom

The number of angular positions obtained was 360, separated $1\pm\eta$ degrees, where η is a variable random error. Reconstruction was made considering the angular projections were obtained with 1 degree angular step in order to see the effect of an error in the angular position has on the final reconstruction.

Figure 6 shows the effect for values of η in the range of $\pm$ 1° and $\pm$3°.
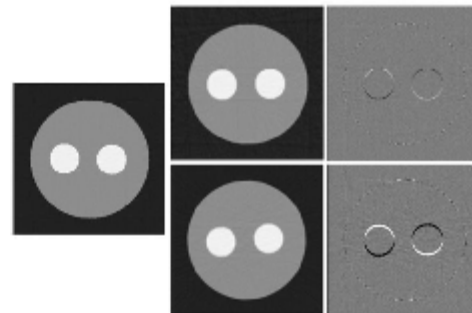
Figure 6. View of the reconstructed image with no errors (left), with an error in the range of ± 1° (top middle) , with an error in the range of ± 3° (bottom middle), sustraction of true image and image with error in the range of ± 1° (top right) and sustraction of true image and image with error in the range of ± 3°(bottom right)

Errors in the angular position lower than 1 degree result on artifacts in the reconstructed images and thoset artifacts increase with the error.

Considering that the resolution we can obtain with the ruler is about 5° (this is the space between mark and mark on the arc), these results indicate the need of a positioning system.

2. Positioning system

We have selected the ADIS16209, a digital inclinometer with an accuracy of 0.1°. To send the analog data obtained by the sensor to the computer we use Arduino Mega, which is an open-source electronics prototyping platform made up of three basic elements: a microcontroller board with inputs and outputs (shown in Figure 7), a development environment or IDE and a programming language.

Figure 7. Platform of Arduino Mega.

Between the inclinometer and Arduino we need an evaluation board to allow for the proper communication. For this purpose we have used the ADIS1620x/PCB evaluation board that provides convenient access to the inclinometer using a standard 2 mm, 2x6, connector interface.

Figure 8 shows the placement of the inclinometer used in the C-Arm.
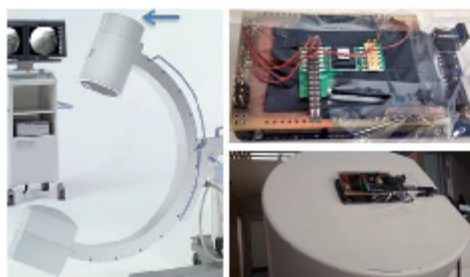
Figure 8. Left: Positioning of the inclinometer in the upper part of the C-arm (blue arrow).Top Right: inclinometer connection with the evaluation board and Arduino board. Bottom right: detail of the placement of the inclinometer to get the right orientation

4.1 Communication between computer and inclinometer.

As explained above, we use Arduino as an intermediary between the inclinometer and computer. First, the inclinometer is connected to Arduino board. Table 1 shows the data configuration for each output data register in the inclinometer.

| Register	Bits	Scale[1]
SUPPLY_OUT	14	0.30518 mV
XACCL_OUT	14	0.24414 mg
YACCL_OUT	14	0.24414 mg
AUX_ADC	12	0.6105 mV
TEMP_OUT	12	−0.47°C
XINCL_OUT[2]	14	0.025°
YINCL_OUT[2]	14	0.025°
ROT_OUT[3]	14	0.025°

[1] Scale denotes quantity per LSB.
[2] Range is −90° to +90°.
[3] Range is −179.975° to +180°.

Table 1. Output Data Register Formats

Each output data register has the following bit sequence: new data (ND) flag, error/alarm (EA) flag, followed by 14 data bits. The ND flag indicates that unread data resides in the output data registers. This flag clears and returns to 0 during an output register read sequence. It returns to 1

after the next internal sample update cycle completes. The EA flag indicates an error condition.

Since we are only interested in data regarding vertical rotation (YINC_OUT register) and horizontal tilt (XINCL_OUT register), we have developed a software using Arduino development environment that records only these data. After reading the content of one of these registers, we mask off the upper two bits (ND and EA), and convert the remaining 14-bit into a decimal equivalent and multiply by 0.025 to convert the measurement into units of angle (°).

4.2 User interaction and data storage

Data cannot be stored in the Arduino for a future use, since it does not offer the possibility of creating a file. Instead, we have implemented a user interface using Processing, which is an open source programming language and integrated development environment based on Java.

The values provided by the inclinometer are in the range of ±90° for the horizontal tilt and ±180° for the vertical rotation In the case of vertical rotation the arc will never exceed the inclinometer's limitation of ±180°. For horizontal tilt the displayed value is not correct for angles with absolute value greater than 90 ° and this error depends on the quadrant the actual angle belongs to, as explained in Table 2.

	Real angle	Angle provided
0°<α<90°	65°	65°
α=90°	90°	90°
90°<α<180°	110°	70°
α=180°	180°	0°
180°<α<270°	200°	-20°
α=270°	270°	-90°
270°<α<360°	300°	-60°
α=360°	360°	0°

Table 2. Examples of desired angles for the horizontal tilt and values obtained with the inclinometer.

The user interface module, apart from saving the data in a text file, solves the problem previously discussed allowing us to visualize the actual position in consecutive angles from 0° to 360°. When the program is initiated, the interface as shown in Figure 9 is displayed.

Figure 9. Interface that appears when the program created in Processing is initiated.

When button "+90" is pressed, the program knows the system is in the situation 90°<α<270°, calculating the angular position as 180-α; when button "+270" is ON the angular position is calculated as 360+α. Also, when the

84

rotation is in the counterclockwise direction the user must use the button "Negative rotation", which will give negative values as shown in Table 3. Each button changes the text inside it from "OFF" to "ON" when is pressed.

In order to improve inaccuracies due to the vibration of the C-arm, we perform an average of the last 10 values read when the system reaches the desired position. The value is saved in the corresponding text file ("Capture" bottom). A different empty file is created each time we start the program.

4.3 Experiments

We have tested the feasibility of using the inclinometer placed on the C-arm in an actual operating room and if its connection interferes the C-arm movements and the normal workflow in a surgical scenario.

We have performed a preliminary experiment checking if values displayed on the computer screen matched the marks in C-arm. First, maintaining the vertical rotation, horizontal tilt was changed, using positive and negative values. We subsequently carried out the same experiment but maintaining the horizontal tilt and moving the vertical rotation. Table 3 shows how values obtained by the inclinometer follow the same trend that those obtained by reading the marks on the arc. We can see also that errors due to manual positioning can be solved by the inclinometer due to higher accuracy.

Counterckwise Horizontal Tilt		Clockwise Horizontal Tilt		Vertical Rotation	
Inclinometer	C-Arm	Inclinometer	C-Arm	Inclinometer	C-Arm
0°	-3°	0°	-9°	90°	93°
-30°	-33°	30°	26°	75°	76°
-60°	-62°	60°	56°	60°	61°
-90°	-83°	90°	88°	45°	46°
-120°	-124°	120°	116°	30°	31°
-150°	-153°	150°	146°	15°	16°
180°	181°	180°	176°	0°	0°
-210°	-214°	210°	205°	-15°	-15°
-240°	-243°	240°	237°	-30°	-38°
-270°	-269°	270°	266°	-40°	-38°
-300°	-304°	300°	297°		
-330°	-334°	330°	328°		
-360°	-363°	360°	357°		

Table 3. Comparison of the angles shown by the arc and the inclinometer at the same position.

1. Discussion and conclusion

We have shown using simulations that even small angular positioning errors lead to artifacts in the reconstructed image, thus indicating the need of a positioning system to obtain higher accuracy using a C-arm. We describe a positioning system based on the ADIS16209 digital inclinometer for the C-arm and positive results from an initial validation.

The main limitation of this preliminary implementation is that we assume that only one of the inclinations is different from zero, thus the values of YINC_OUT or XINC_OUT are directly the positioning angles. When moving the C-arm to a different plane in which both are different from zero, the values for both inclinations should be calculated combining the information given by both parameters of the inclinometer. After implementing this feature, future will also include using the inclinometer on the C-arm to take real data and calibrate the mechanical misalignments to obtain a reconstructed image. Furthermore, we will increase the accuracy of the values shown in the screen using all significant digits provided by the inclinometer.

References

1. Calvo F., et al., Radioterapia intraoperatoria: desarrollo metodológico y experiencia clínica inicial. Oncología 1997;20(7):435-43. Oncología, 1997. 20(7): p. 435-43

2. Desco, M., et al., Simulated Surgery on Computed Tomography and Magnetic Resonance Images: An Aid for Intraoperative Radiotherapy. Comput Aided Surg, 1997. 2(6): p. 333-9.

3. Pascau, J., et al., An Innovative Tool for Intraoperative Electron Beam Radiotherapy Simulation and Planning: Description and Initial Evaluation by Radiation Oncologists. Journal of Radiation Oncology, Biology, Physics, 2012. 83(2): p. e287-e295.

4. Dawson, L.A. and D.A. Jaffray, Advances in image-guided radiation therapy. J Clin Oncol, 2007. 25(8): p. 938-46.

5. Xing, L., et al., Overview of image-guided radiation therapy. Med Dosim, 2006. 31(2): p. 91-112.

6. Cho, Y., et al., Accurate technique for complete geometric calibration of cone-beam computed tomography systems. Med. Phys., 2005. 32(4): p. 968-83.

7. M Paraiso, C de Molina, J Pascau, M Desco, M Abella. Evaluation of the effect of calibration accuracy in a C-arm for its use in tomography. "Evaluation of the effect of calibration accuracy in a C-arm for its use in tomography". Libro de Actas XXX CASEIB 2012, s.p., 2012.

8. C de Molina, J Pascau, M Desco, M Abella. Calibration of a C-arm X-ray system for its use in tomography

9. Abella, M., et al., Software Architecture for Multi-Bed FDK-based Reconstruction in X-ray CT Scanners. Computer methods and programs in biomedicine, 2012. 107(2): p. 218-32.

GLOSSARIUM

- **ALARA**: As Low As Reasonably Achievable
- **CASEIB**: Congreso Anual de la Sociedad Española de Ingeniería Biomédica
- **CR**: Computed Radiography
- **CT**: Computed Tomography
- **CUDA**: Compute Unified Device Architecture
- **DR**: Direct Radiography
- **FBP:** Filtered Backprojection
- **FDK**: Feldkamp, David y Kreis
- **FFT:** Fast Fourier Transform
- **FOV**: Field of View
- **FPD:** Flat Panel Detector
- **GPU**: Graphic Processing Units
- **ICU:** Intensive Care Unit
- **IRD**: Image Reader Device
- **KeV**: Kiloelectron volt
- **KVp**: Peak Kilovoltage
- **LIM**: Laboratorio de Imagen Médica
- **mAs**: Milliampere-second
- **MATLAB:** Matrix Laboratory
- **MEMS**: Microelectromechanical systems
- **PACS**: Picture Archiving and Communication System
- **PCB**: Printed Circuit Board
- **PSP**: Photostimulable storage phosphor imaging plate
- **ROI**: Region Of Interest
- **SDD**: Source to Detector Distance
- **SEDECA**L: Sociedad Española de Electromedicina y Calidad
- **SPECT**: Single-Photon Emission Computed Tomography
- **SPI**: Serial Peripheral Interface
- **TAC**: Tomografía Axial Computarizada
- **UMCE**: Unidad de Medicina y Cirugía Experimental
- **UCI**: Unidad de Cuidados Intensivos
- **XRII**: X-Ray Image Intensifier

BIBLIOGRAPHY

[1]   "Handbook of Medical Imaging, Volume 1. (Parts 1 and 2) Physics and Psychophysics (SPIE Press Monograph Vol. PM79/SC): 9780819477729: Medicine & Health Science Books @ Amazon.com." [Online]. Available: http://www.amazon.com/Handbook-Medical-Imaging-Psychophysics-Monograph/dp/0819477729. [Accessed: 16-Jun-2015].

[2]   "Medical Image Processing, Reconstruction and Restoration: Concepts and Methods (Signal Processing and Communications): 9780824758493: Medicine & Health Science Books @ Amazon.com." [Online]. Available: http://www.amazon.com/Medical-Image-Processing-Reconstruction-Restoration/dp/0824758498. [Accessed: 16-Jun-2015].

[3]   P. Suetens, *Fundamentals of medical imaging*. 2009.

[4]   A. C. and M. S. Kak, "principles of Computerized Tomographic," 2001.

[5]   H. Turbell, *Cone-Beam Reconstruction Using Filtered Backprojectionn*, no. 672. 2001.

[6]   J. F. Barrett and N. Keat, "Artifacts in CT: recognition and avoidance.," *Radiographics*, vol. 24, no. 6, pp. 1679–91, Jan. 2004.

[7]   "Mobile X-ray Image Intensifier System Mobile X-ray Image Intensifier System."

[8]   A. Devices, "iSensor ^{TM} Inclinometer / Accelerometer Evaluation Board ADIS1620x / PCB," 2007.

[9]   S. Vedantham, A. Karellas, S. Suryanarayanan, D. Albagli, S. Han, E. J. Tkaczyk, C. E. Landberg, B. Opsahl-Ong, P. R. Granfors, I. Levis, C. J. D'Orsi, and R. E. Hendrick, "Full breast digital mammography with an amorphous silicon-based flat panel detector: physical characteristics of a clinical prototype.," *Med. Phys.*, vol. 27, no. 3, pp. 558–67, Mar. 2000.

[10]   PerkinElmer, "XIS Reference Book - X-Ray Imaging Software Table of Contents," pp. 1–131, 2010.

[11]   G. Dougherty, *Digital image processing for medical applications*. 2009.

[12]   C. Solomon, *Fundamentals of digital image processing*. 2011.

[13]   D. A. Jaffray, J. H. Siewerdsen, J. W. Wong, and A. A. Martinez, "Flat-panel cone-beam computed tomography for image-guided radiation therapy.," *Int. J. Radiat. Oncol. Biol. Phys.*, vol. 53, no. 5, pp. 1337–49, Aug. 2002.

[14]   Y. Cho, D. J. Moseley, J. H. Siewerdsen, and D. A. Jaffray, "Accurate technique for complete geometric calibration of cone-beam computed tomography systems," *Med. Phys.*, vol. 32, no. 4, p. 968, Mar. 2005.

[15]   M. J. Daly, J. H. Siewerdsen, Y. B. Cho, D. A. Jaffray, and J. C. Irish, "Geometric calibration of a mobile C-arm for intraoperative cone-beam CT.," *Med. Phys.*, vol. 35, no. 5, pp. 2124–36, May 2008.

[16] T. A. W. and T. J. R. Noo, F. R. Clackdoyle, C. Mennessier, "An analytic method based on identification of ellipse parameters for scanner calibration in conebeam tomography," 2000.

[17] M. Körner, C. H. Weber, S. Wirth, K.-J. Pfeifer, M. F. Reiser, and M. Treitl, "Advances in digital radiography: physical principles and system overview.," *Radiographics*, vol. 27, no. 3, pp. 675–86, Jan. .

[18] J. Hsieh, *Computed Tomography: Principles, Design, Artifacts, and Recent Advances*. SPIE Press, 2003.

[19] M. D. and J. J. V. Abella, M, "Contributions to Image Reconstruction in High-Resolution Multimodality Systems for Preclinical Applications," 2010.

[20] M. Abella, J. J. Vaquero, A. Sisniega, J. Pascau, A. Udías, V. García, I. Vidal, and M. Desco, "Software architecture for multi-bed FDK-based reconstruction in X-ray CT scanners.," *Comput. Methods Programs Biomed.*, vol. 107, no. 2, pp. 218–32, Aug. 2012.

[21] Y. Sun, Y. Hou, F. Zhao, and J. Hu, "A calibration method for misaligned scanner geometry in cone-beam computed tomography," *NDT E Int.*, vol. 39, no. 6, pp. 499–513, Sep. 2006.

[22] P. T. Data, "High Accuracy , Dual-Axis Digital Inclinometer & Accelerometer," *Nonlinearity*, 2007.